A Geometric Approach to Modeling Microstructurally Small Fatigue Crack Formation: II. Simulation and Prediction of Crack Nucleation in AA 7075-T651

J D Hochhalter, D J Littlewood, R J Christ Jr., M G Veilleux, J E Bozek, A R Ingraffea, and A M Maniatty

Abstract. The objective of this paper is to develop further a framework for computationally modeling microstructurally small fatigue crack growth in AA 7075-T651 [1]. The focus is on the nucleation event, when a crack extends from within a second-phase particle into a surrounding grain, since this has been observed to be an initiating mechanism for fatigue crack growth in this alloy. It is hypothesized that nucleation can be predicted by computing a non-local nucleation metric near the crack front. The hypothesis is tested by employing a combination of experimentation and finite element modeling in which various slip-based and energy-based nucleation metrics are tested for validity, where each metric is derived from a continuum crystal plasticity formulation. To investigate each metric, a non-local procedure is developed for the calculation of nucleation metrics in the neighborhood of a crack front. Initially, an idealized baseline model consisting of a single grain containing a semi-ellipsoidal surface particle is studied to investigate the dependence of each nucleation metric on lattice orientation, number of load cycles, and non-local regularization method. This is followed by a comparison of experimental observations and computational results for microstructural models constructed by replicating the observed microstructural geometry near second-phase particles in fatigue specimens. It is found that orientation strongly influences the direction of slip localization and, as a result, influences the nucleation mechanism. Also, the baseline models, replication models, and past experimental observation consistently suggest that a set of particular grain orientations is most likely to nucleate fatigue cracks. It is found that a continuum crystal plasticity model and a non-local nucleation metric can be used to predict the nucleation event in AA 7075-T651. However, nucleation metric threshold values that correspond to various nucleation governing mechanisms must be calibrated.

1. Introduction

Recent efforts to reduce the costs associated with overly conservative fatigue life estimates have motivated the investigation of using specific knowledge of the fatigue process, together with novel sensors and sophisticated reasoning techniques, to create predictive models of fatigue damage [2]. This prognosis approach requires a detailed treatment of the microstructurally small fatigue crack (MSFC) growth phase because researchers have found that the time spent in the MSFC phase accounts for 50–70% of total fatigue life [3, 4]. Suresh asserted that up to 90% of the total fatigue life of a structural component could be consumed during the formation of a dominant fatigue crack [5]. Therefore, simulating the MSFC phase is a major component of structural reliability estimates in a prognosis system. Such prognosis systems are especially needed for typical in-service aircraft components and materials, and as such, Aluminum Alloy (AA)7075-T651 was chosen as the case study alloy for this research.

The MSFC phase of fatigue is strongly dependent on microstructural heterogeneities and particle inclusions, which have long been the focus of fatigue-life studies for aluminum alloys. In many aluminum alloys, the MSFC phase consists of three distinct stages: incubation, nucleation, and microstructurally small crack propagation. Each stage is strongly dependent on characteristics of the local microstructure. For AA 7075-T651, the incubation phase is dominated by the cracking of Al_7Cu_2Fe particle inclusions [1, 6]. The nucleation event is herein defined by the extension of a crack, initially contained within a particle inclusion, into the surrounding matrix material. Microstructurally small propagation is defined as the early stage of crack growth in which microstructural features play a dominate role in controlling crack shape and rate of growth.

The overall objective of the present series of papers is to describe the development and validation of a computational simulation methodology capable of reproducing the mechanics and probabilistic nature of MSFC formation. In the first paper of the present series, Bozek *et al.* quantified the stochastic nature of the incubation stage of AA 7075-T651 by developing a methodology to predict the percentage of cracked particles by accounting for variation in particle size, shape, location, strain level, and surrounding grain orientation [1]. That methodology provides a statistical distribution of second-phase particles that are likely to incubate a crack during the initial load cycle, given a distribution of idealized uncracked second-phase particles and the orientation of the surrounding grain.

The present paper focuses on the nucleation stage of MSFC. It is hypothesized that the crack nucleation event can be predicted by computing a non-local nucleation metric near the crack front. A major objective is to determine the manner in which slip localizes and accumulates over applied load cycles and the effect of microstructure on that accumulation. A crystal elastic-viscoplastic material model is used to compute slip, and is discussed in Section 2. Crack nucleation is believed to be a function of slip localization and accumulation near an incubated crack front during fatigue loading. This accumulation occurs due to the formation of dislocation structures during plastic deformation.

Five candidate nucleation metrics are investigated that were either found to be applicable from the literature or formulated for the purpose of the present study. Three of the metrics are solely functions of plastic slip, one is an energy-based nucleation metric, and the last is based on both plastic deformation and stress. Formulations and motivations for each of the five nucleation metrics are presented in Section 2. In Section 3, a baseline model is studied to illustrate the dependence of each nucleation metric on lattice orientation and cyclic load history. In addition, Section 3 includes the methodology used for non-local sampling and regularization calculations in the presence of

singularities at the crack front. The modeling approach is then applied to realistic microstructural models constructed directly from microscopy data in Section 4. Finally, results of the study and similarities between computational modeling and experimental observations are discussed.

The study and corresponding discussion are mainly qualitative; a statistical representation of the threshold values of the five nucleation metrics and their association with underlying nucleation mechanisms are not considered here. The objective is to understand the relative differences in general applicability and numerical qualities among the five nucleation metrics and two non-local methods investigated. Results of the present study will be used in subsequent work for the implementation of a nucleation filter capable of identifying particles that are likely to nucleate fatigue cracks. A 'nucleation filter' will then be applied to calculate statistical realizations of crack nucleation sites as a function of a nucleation metric, surrounding grain orientation, local strain level, and particle shape.

1.1. Background

It is commonly observed during experiment that microstructure plays a dominant role in MSFC behavior [1, 7–16]. Murakami *et al.* observed that microstructure can enforce variability of the fatigue crack threshold value, ΔK_{th}, and that this variability was upwards of 100% within neighboring grains [7]. Taylor concluded similarly from fatigue experimentation that the behavior of microstructurally small cracks is highly variable [8]. Taylor attributed this variability to microstructural inhomogeneity and manufacturing-related residual stresses near the crack tip.

The effect of microstructure on MSFC behavior is material dependent. Patton *et al.* observed the effect of lattice orientation on crack formation in AA 7010 [10]. It was observed that crack nucleation was most likely to occur within a grain in a twisted-cube orientation, which they defined as a "grain orientation for which the two highest Schmid factors are comparable and relatively large." They also found that cracks grew along {111}, {110}, or {100} crystallographic planes. Similarly, Oja *et al.* observed, for Waspaloy (an FCC nickel-based superalloy), that nine of ten observed microstructurally small cracks nucleated within a group of grains that all had comparable and relatively large Schmid factors [17]. Gupta used crystallography to quantify the MSFC facets in AA 7075-T651 and 7050-T7451, which indicated absence of stage I fatigue crack growth near the second-phase particles that nucleated a crack: crack growth did not correspond to any {111} planes [18]. Furthermore, facet crystallography revealed that crack facet normals were often parallel to the RD, which was the loading direction in that work [18]. Therefore, it is expected herein that the nucleation directions will not coincide with the {111} planes.

McDowell *et al.* identified the distinct stages of the MSFC phase and implemented a corresponding series of phenomenological models to predict the fatigue life of A356-T6 [19]. Following on that work, localized material response in the neighborhood of an inclusion was studied by Gall, Xue, and Zhang [20–22]. Gall studied the cases of cracked and debonded particles embedded within an isotropic elastic-plastic region and found that strain localization, predicted using 2-D models, is comparable between the two cases. In addition, it was determined that particle size and loading ratio are more significant than particle shape in the nucleation of fatigue cracks. Size effect was incorporated by fixing a non-local regularization area from which to calculate driving parameters, independent of crack size. This is a viable approach if the domain over which the dominant mechanisms act is known, *a priori*. Xue *et al.* used an internal state variable, isotropic, elastic-plastic constitutive model for non-local calculation of the maximum plastic shear strain amplitude, which was used to inform a modified Coffin-Manson model to characterize incubation

life. In that work, parameters for considering grain orientation and size effects were included, but ultimately not used because of lack of information on the complex effect these factors may have. Zhang *et al.* studied fatigue crack nucleation from inclusions within an isotropic elastic-plastic rate-independent material using 3-D finite element modeling [22]. While these models recognize and incorporate the important influence of particle inclusions in crack incubation and nucleation, they do not consider the importance of the grain morphology or orientations on the nucleation process.

A few studies have incorporated the effect of grain morphology or orientations on MSFC. Patton *et al.* modeled the dependence of crack nucleation and propagation on grain structure [10]. The objective of that work was to determine the effects of grain boundaries and the volume fraction of recrystallized grains on total fatigue life for AA 7010. Patton *et al.* deduced that incorporation of the number of cycles to incubation and nucleation (the combination was referred to as initiation in that paper) could improve the proposed fatigue life model. Morris and James built on the work of Chang *et al.* by incorporating the calculation of an effective shear stress, constant within each grain, that considered crystallographic orientation of the grains with particle inclusions [15]. Using Monte Carlo simulations, they determined that nucleation would occur at progressively smaller particles throughout fatigue life. Also, it was found that crystallographic orientation was a major factor in the probability of nucleation of an incubated crack.

Bennett and McDowell considered the effect of crystallographic orientation on three proposed fatigue crack initiation parameters. They modeled an idealized, planar polycrystal without inclusions subjected to several different cyclic loading histories, considering a combination of plane strain tension/compression and shear [23]. They incorporated the predicted distributions of the fatigue crack initiation parameters, computed from a single hysteresis loop, into a fatigue crack growth equation, and correlated the predictions with measurements of a MSFC length distribution in a steel with a martensitic-ferritic microstructure. Because of the 2-D idealization of the grain structure, crystal plasticity formulation, and boundary conditions, the results of their work are qualitative in assessing the influence of microstructure.

Kalnaus and Jiang and Korunsky *et al.* investigated the effect of grain orientations on total fatigue life [24,25]. Kalnaus and Jiang proposed a damage metric associated with energy dissipation on a critical slip plane for single crystal copper, and obtained good agreement with single slip, fully reversed, strain-controlled experiments. Korunsky *et al.* computed the maximum energy dissipated in a cycle for a 3-D polycrystal (without particles) with smeared grain boundaries, and obtained good correlation with fatigue life for a nickel-based superalloy.

The present study extends upon these prior works by incorporating fully 3-D microstructural models containing cracked particles, polycrystal elastic-viscoplasticity, and validation through finite element models that replicate observed microstuctures. The effect of the grain orientations and grain structure in the vicinity of cracked particles is explicitly modeled. The incorporation of the polycrystal elastic-viscoplasticity allows for the modeling of individual slip systems which enables the computation of more accurate fields. This addition to previous modeling studies provides the capability to explore specific underlying mechanisms of the nucleation stage, such as orientation-dependent localized slip, and improves understanding of the effects of lattice orientation and various local heterogeneities on the MSFC phase of total fatigue life.

An alternative approach to representing fundamental mechanisms active during nucleation is provided by discrete dislocation modeling. Explicitly modeling dislocations and the interactions between them naturally simulates the mechanisms leading to slip localization. In contrast, in this paper slip localization is a homogenization of dislocation activity within a continuum crystal plasticity formulation. In a recent paper by Groh *et al.*, a cracked elastic particle within a

surrounding ductile matrix, analogous to the baseline model presented in this paper, was modeled using the discrete dislocation modeling approach presented by Cleveringa *et al.* [26, 27].

1.2. Experiment

For this study, fatigue experiments of AA 7075-T651 double edge-notched (DEN) specimens were carried out to provide observations of the MSFC phase. A detailed explanation of the experiments completed that support this work is given by Payne *et al.* [6]. The fatigue experiment is briefly overviewed here to highlight the experimental observations that formed the basis for the computational modeling completed in this study.

Figure 1 illustrates the DEN specimen and notch root from which data were taken throughout 3000 cycles of $R = 0.1$ constant amplitude loading. The coordinate axes correspond to the rolling direction (RD), normal direction (ND), and transverse direction (TD). Loading was applied in the RD. The observation window at the monitored notch root was 1.50 mm x 0.50 mm in ND and RD, respectively. A small portion of the observation window is shown in the center of Figure 1. One of the second-phase particles within that window is shown at the right of Figure 1. Incubation, nucleation, and microstructurally small propagation were observed to occur at that particle and are denoted by (i), (ii), and (iii), respectively. Electron Backscatter Diffraction (EBSD) was used to provide the grain geometry and orientations shown in Figure 1. Overlaying the EBSD with the observed crack path illustrates the influence of the local microstructure on the crack growth.

This experiment showed that the *incubation stage* in AA 7075-T651 occurs, almost exclusively, during manufacturing or the first half cycle of loading, but only in a small percentage of particles in a highly stressed region [1]. However, the number of cycles to crack incubation is strongly dependent on the applied loading. In a joint study, Weiland *et al.* observed that the onset of incubation occurred between 100 and 1000 cycles in AA 7075-T651 match-stick specimens with $R = 0$ cyclic loading. One cause for this difference in the number of cycles to incubation is due to the difference in maximum stress concentration [16]. Also, the electro-polishing technique used by Weiland *et al.* is known to have a significant influence on the number of cycles to incubation [28].

In the DEN experiments completed by Payne *et al.*, it was observed that the small percentage of Al_7Cu_2Fe particles that crack under loading generally has an average observable surface area of 17-46 μm^2, where the overall average observable surface area of all Al_7Cu_2Fe particles was 10-11 μm^2, see Table 2 in [6]. These observations are consistent with those of many others [10–12, 16, 21, 29]. In other aluminum alloys, second-phase particles are also the site of crack incubation. However, the incubation mechanism for other aluminum alloys can also include particle debonding, which is not the mechanism of consequence in AA 7075-T651 [1, 16, 19, 20, 30].

Experimental data showing the number of load cycles at which *nucleation events* were observed in the present study are presented in Figure 2. Crack nucleation was found to occur at approximately 73% of the cracked particles and required, at most, 300 load cycles, less than 10% of the total fatigue life. Also, it was observed that crack nucleation occurred exclusively at cracked particles and that no nucleation occurred at debonded particles. This observation was also made by Weiland *et al.* [16]. Furthermore, Figure 2 shows that the nucleation event often occurred in the range of 10 to 100 load cycles, less than 3% of total fatigue life. In addition, the size of the cracked particle did not correlate with the likelihood that a crack would nucleate or with the length of nucleated cracks. Therefore, particle size alone is not a sufficient metric for simulating crack nucleation or propagation. Furthermore, Gupta observed that relatively large particles were associated with relatively broad, flat crack nucleation facets; small particles were associated with smaller, stepped
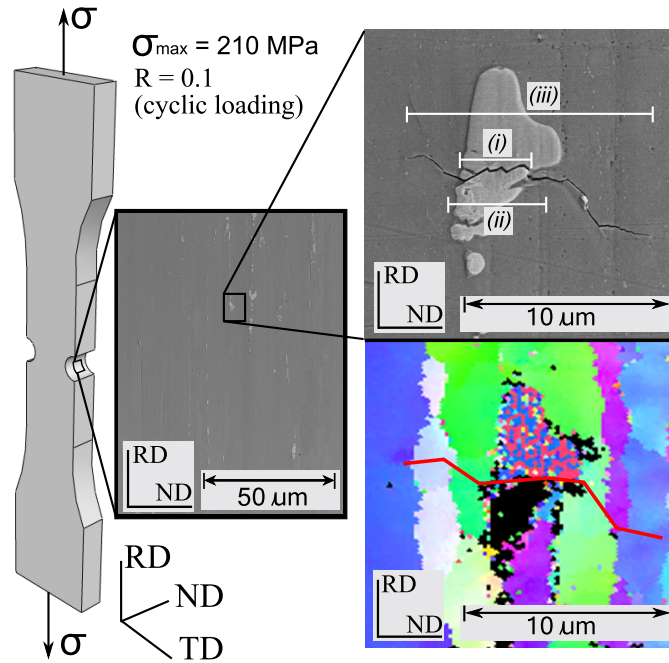
Figure 1. Double edge-notched specimen with cyclic loading applied in the RD (left). Observation window at notch root in which scanning electron microscopy was used to track the stages of MSFC throughout 3000 load cycles to track MSFC phase (center). Cracked Al_7Cu_2Fe particle inclusion at 3000 load cycles, and corresponding grain orientations, in AA 7075-T651 that has undergone (i) incubation, (ii) nucleation, and (iii) microstructurally-small propagation (right).

facets. That observation led to the speculation that varying levels of strain accumulation near the incubated crack front strongly influence the MSFC behavior [18]. In the present study it is hypothesized that, in addition to particle geometry, the surrounding microstructure governs the localization and accumulation of slip, which drives the nucleation event.

The lattice orientations of the grains surrounding the particle inclusion, at the right in Figure 1, are shown using orientation imaging micrography. On average, the crack is propagating through the surrounding grains in a plane perpendicular to RD, which is aligned with the loading direction. However, there are marked changes in crack trajectory at grain boundaries that illustrate the microstructural effect on crack growth direction during the propagation stage of MSFC growth. Similar observations are reported in the literature for A356, AA2000 series, AA7000 series, and Al-Li alloys [9, 11, 16, 21, 30–33].

2. Nucleation Metrics

Fatigue crack nucleation in AA 7075-T651 is preceded by localized plastic slip in the neighborhood of a cracked particle inclusion. AA 7075-T651 (peak-aged temper) is strengthened by non-shearable precipitates about which Orowan dislocation loops form during plastic deformation. As a result of these barriers to dislocation motion, the plastic deformation at heterogeneities, in this case cracked
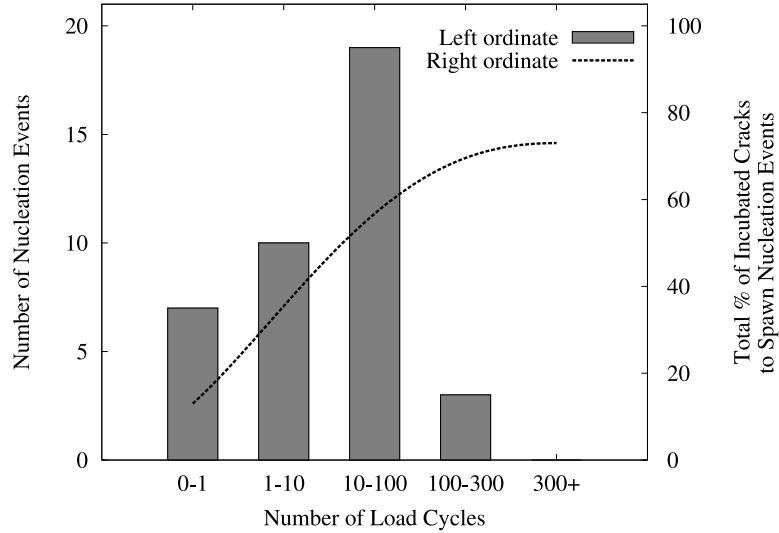
Figure 2. A histogram of the cycles at which nucleation events occurred for the AA 7075-T651 DEN specimen. Approximately 73% of the observed incubated cracks led to nucleated cracks into a surrounding grain.

particles, is relatively diffuse with multiple slip systems active and a greater degree of irreversibility of slip than in underaged alloys. Persistent slip bands (PSBs) do not appear to form in AA 7075-T651, and fatigue cracks are nucleated more rapidly relative to materials where PSBs are observed. Because of the diffuse plasticity, the nucleation mechanism may be similar to that in low cycle fatigue where the plastic zone is larger. However, the actual mechanism of fatigue crack nucleation is not known, and thus, several candidate nucleation metrics are explored in this work.

The observations described in the previous section motivate the five candidate nucleation metrics investigated in this study. Three metrics are based exclusively on crystallographic slip, one on the energy dissipated during crystallographic slip, and one on a combination of slip and normal stress on a slip plane. In this work, an elastic-viscoplastic crystal model is used with a standard power law relationship between the rate of shearing and resolved shear stress on the slip systems, and the hardening behavior is modeled based on the Orowan looping mechanism. The slip and stress state are computed directly from the integration of the constitutive equations throughout a finite element model of a microstructure. For a more complete discussion of the material and computational model, the reader is referred to Bozek *et al.* and Matouš and Maniatty [1, 34].

The first three nucleation metrics are based on the observation that the local cyclic plastic slip at a cracked particle leads to crack nucleation. This is the motivation of the Coffin-Manson type relationship used in McDowell *et al.* and Xue *et al.* [19, 21]. In that work, crystal plasticity in the matrix material is not considered, and the amplitude of the maximum plastic shear strain over a cycle is related to the number of cycles to nucleate a crack. In Bennett and McDowell, a simple 2-D polycrystal model with two slip systems is considered, and the maximum shear strain amplitude on either of the slip systems is investigated as a potential crack initiation metric [23]. In the present study, a 3-D polycrystal is modeled and all twelve primary {111}<110> slip systems (four slip

planes each with three slip directions) for FCC crystals are considered. Plastic deformation in the matrix material is due to slip on the crystallographic slip systems. The plastic velocity gradient, $\hat{\mathbf{L}}^p$, is related to the rate of slip on the slip systems as

$$\hat{\mathbf{L}}^p = \sum_{\alpha=1}^{N_s} \dot{\gamma}^\alpha \mathbf{P}^\alpha, \tag{1}$$

where α denotes a specific slip system, N_s the total number of slip systems, $\dot{\gamma}^\alpha$ the slip rate on slip system α, and $\mathbf{P}^\alpha$ the Schmid tensor for slip system α. A power law relates $\dot{\gamma}^\alpha$ to the resolved shear stress on each slip system. Given that there are twelve slip systems and four slip planes, the question that arises is: What is an appropriate measure of slip to use as a metric for fatigue crack nucleation? The first three nucleation metrics define candidate measures to be investigated.

Nucleation metrics D_1, D_2, and D_3 are functions of accumulated slip γ^α, which is computed for slip system α as

$$\gamma^\alpha = \int_0^t |\dot{\gamma}^\alpha|\, dt. \tag{2}$$

It should be noted that the accumulated plastic slip defined above, when tracked as a function of time, can be directly related to the plastic slip amplitude for any given cycle. Nucleation metric D_1 is the maximum value of γ^α over each of the slip systems,

$$D_1 = \max_\alpha \gamma^\alpha. \tag{3}$$

D_2 is the maximum value of total accumulated slip over each slip plane,

$$D_2 = \max_p \gamma^p, \tag{4}$$

where the total slip on slip plane p, γ^p, is computed as the scalar sum of the accumulated slip for the slip systems on plane p. Nucleation metric D_3 is the total accumulated slip over all slip systems,

$$D_3 = \gamma = \sum_{\alpha=0}^{N_s} \gamma^\alpha. \tag{5}$$

If slip on a single slip system dominates, all three of these metrics will give similar results. Nucleation metric D_2 identifies a critical plane on which the total slip contributes to fatigue crack nucleation, and nucleation metric D_3 is based on the proposition that multi-slip occurs and the slip on all of the slip systems contributes to fatigue crack nucleation.

Nucleation metric D_4 assumes crack nucleation is associated with energy dissipation due to plastic slip on a slip plane. Skelton suggested that the energy dissipated per each saturated cycle could be associated with the energy necessary to propagate a crack [35]. Korunsky *et al.* proposed an energy dissipation criterion in the context of a crystal plasticity model that considered the energy dissipated over all the slip systems for a saturated loading cycle in a nickel-based superalloy [25]. The energy dissipation per cycle was found to correlate well with the number of cycles to failure. In the present study, nucleation metric D_4 is the maximum value of energy dissipated on a given slip plane during the course of plastic deformation,

$$D_4 = \max_p \int_0^t \sum_{\alpha=0}^{N_d} |\dot{\gamma}_p^\alpha \tau_p^\alpha|\, dt, \tag{6}$$

where τ^α is the resolved shear stress along slip system α and N_d is the total number of slip systems on a given slip plane. Kalnaus and Jiang proposed a fatigue damage metric for copper single crystals

that contains the above term as well as a term associated with the energy dissipation normal to the slip plane [24]. The term associated with the energy dissipation normal to the slip plane was found to be relatively small on the critical plane. The damage accumulation metric in Kalnaus and Jiang was found to correlate well with four different sets of experimental data on copper single crystals. By tracking metric D_4 with time, the energy dissipated due to slip on a critical plane over each cycle may also be determined.

The importance of the normal stress on the critical plane of maximum shear strain has been identified in earlier works, and is considered in metric D_5. Fatemi and Socie demonstrated that the normal stress on the plane of maximum shear strain amplitude influences Stage I fatigue crack propagation and proposed a fatigue crack nucleation criterion that includes a combination of maximum shear strain amplitude and maximum normal stress on the plane of maximum shear strain amplitude [36]. That work follows the methodology of the earlier work of Brown and Miller [37]. More recently, Tschopp *et al.* studied the effect of normal stress on the nucleation of dislocation loops in copper single crystals using atomistic simulations, and found that a tensile normal stress on the slip plane greatly lowers the shear stress required to nucleate a dislocation loop, which suggests a source of the normal stress effect observed by Fatemi and Socie [38]. Nucleation metric D_5 is a modification of the metric presented by Fatemi and Socie and considers the combined effect of crystallographic slip and tensile stress on a slip plane,

$$D_5 = \max_p \int_0^t \sum_{\alpha=0}^{N_d} |\dot{\gamma}_p^\alpha| \left(1 + k \frac{\langle \sigma_n^p \rangle}{g_o}\right) dt, \tag{7}$$

where $\langle \sigma_n^p \rangle$ is the tensile stress on slip plane p ($\langle \cdot \rangle$ are Macaulay brackets defined such that $\langle x \rangle = 0$ if $x \leq 0$ and $\langle x \rangle = x$ if $x > 0$ so that only tensile stress has an effect), g_o is the initial hardness (resistance to slip) on the slip systems, and the parameter k, set to 0.5 in the present study as suggested by Fatemi and Socie, dictates the importance of tensile stress relative to plastic slip [36]. Bennett and McDowell and Zhang *et al.* also investigated a metric similar to this as a potential crack initiation metric [22, 23].

3. Baseline Study

A baseline model was defined to study the effect of orientation on the nucleation event using the nucleation metrics discussed in Section 2, within the finite element framework. The baseline model used in this paper is similar to that used by Bozek *et al.* [1]. Figure 3 illustrates the geometry and boundary conditions used. All elements within this study are 10-node, hybrid tetrahedral elements. The baseline model emulates a grain that is located at the surface of a notch root of a DEN specimen containing a second-phase surface particle. An elastic-plastic finite element analysis of the full DEN specimen, Figure 1, was completed and local strain fields extracted to obtain an accurate description of the strain field local to each notch; a local peak strain field of 1% in the RD was computed [39]. The boundary conditions applied to the baseline model are such that:

(i) the face containing the characteristic surface particle, corresponding to the surface of the edge notch root, is modeled as a free surface;

(ii) the two faces that are normal to the RD have prescribed displacement boundary conditions such that 1% strain is applied in the RD at load cycle peaks; and

(iii) each of the remaining faces of the hexahedral grain is constrained against displacement in its local normal direction.

Table 1. Rodrigues parameters for A, B, and C lattice orientations.

Orientation label	Rodrigues parameters (r_1, r_2, r_3)
A	(0.0, 0.0, 0.2101)
B	(0.0858, 0.2071, -0.2071)
C	(-0.2071, 0.4142, -0.0858)
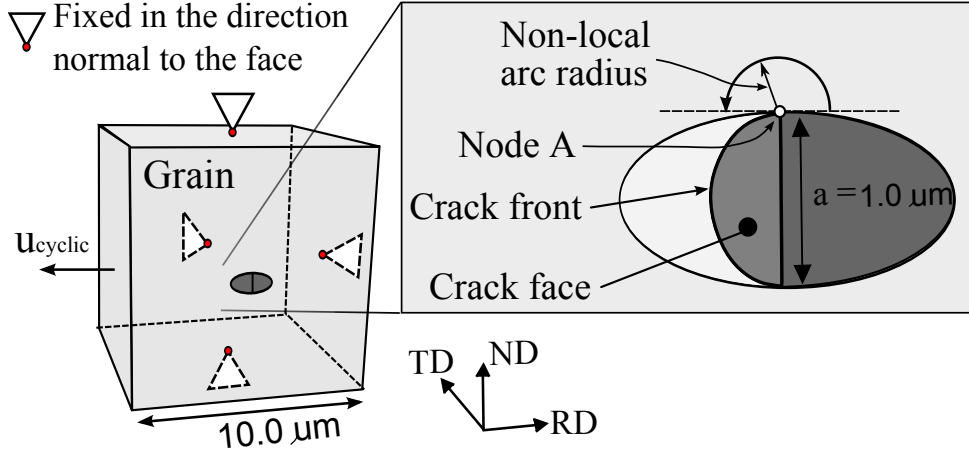
Figure 3. Single-grain single-particle baseline model configuration. A non-local arc in the RD-ND plane is shown centered on Node A. In the detailed area surrounding the ellipsoidal particle, the left half of the particle is transparent to reveal the crack front and crack face. The crack face is in the TD-ND plane.

The hexahedral region, representing a grain, is modeled using the polycrystal elastic-viscoplastic material model discussed in Bozek *et al.* and Matouš and Maniatty [1, 34]. The ellipsoidal region, representing a characteristic second-phase particle, is linear elastic and cracked along its midplane — normal to the RD. The idealized cracked particle is centered on an RD-ND free surface of the surrounding hexahedral grain. In the detailed region of Figure 3, the left half of the particle is removed to reveal the crack front and crack face. Also illustrated is a non-local arc about Node A from which the nucleation metrics were queried. For a complete discussion of inherent assumptions and verification of the baseline model, the reader is directed to [1].

Five cycles of R=0.1 loading were applied to the baseline model, simulating local loading conditions in the DEN specimen, for the three distinct grain orientations (defined as Rodrigues parameters) given in Table 1. Orientation A is similar to the "Low stress" orientation defined by Bozek *et al.* in that a particle is under relatively low stress when surrounded by a grain in this orientation [1]. However, Orientation A is also a twisted-cube orientation as defined by Patton *et al.* [10]. Orientation A was analyzed to investigate the observations made by Patton *et al.* discussed in Section 1.1. Orientations B and C are equivalent to the "Intermediate stress" and "High stress" orientations, respectively, as defined by Bozek *et al.* [1].

3.1. Finite Element Analysis and Non-local Nucleation Metrics

Each nucleation metric, $D_{1...5}$, is computed at each gauss point within the hexahedral grain in the baseline finite element model. However, the presence of the sharp crack front causes a singularity of $D_{1...5}$ along the crack front. The form of the singularity in the crystal elastic-viscoplastic grain material is unknown. Rice *et al.* showed that the form of the singularity changes with respect to the angle about the crack tip in the presence of slip systems [40]. Currently, there is no finite element scheme to account for this singularity in general, as is done, for example, with quarter-point elements in linear elastic fracture mechanics. Therefore, non-local regularization must be used near the crack front. Such non-local regularization introduces additional parameters that must be studied, *e.g.* non-local domain and regularization method.

The size of the non-local domain has been considered in several related studies. Gall *et al.*, in a study of MSFC growth from debonded, second-phase inclusions in A356 aluminum alloy, used a non-local domain area between $0.012D^2$ and $0.0625D^2$, where D is the maximum dimension of the modeled particle [20]. This domain area range corresponds to a square with sides of length 10–25% of D. Xue *et al.* defined a non-local averaging volume, which was asserted to be 1% of the volume of the particle in a study of MSFC growth in AA 7075-T651 [21]. Similarly, Zhang *et al.* defined a non-local averaging volume, which was asserted to be 10% of the volume of the smallest particle modeled in a study of MSFC growth in shot-peened martensitic steel [22]. In each of those studies, either a non-local area or volume, which included the singular region immediately adjacent to the crack was defined and sampled. Unlike previous studies, sampling very near the crack front is avoided here: finite element results are too unreliable there. In this study, an arc is used, illustrated in Figure 3, rather than an areal or volume sampling. In preliminary simulation experiments, this approach was found to provide significantly improved mesh convergence rates. Also, to assert that the non-local domain size depends on particle volume dictates that non-local domain size is somewhat independent of the incubated crack size. For example, a particle with aspect ratio 1:2:1 (RD:ND:TD) and another with ratio 2:1:1 (RD:ND:TD) have the same volume, but the incubated crack dimension, a, of the first particle would be twice that of the second for the baseline model studied here. Here, the non-local domain size is defined to scale with the process zone size. Therefore, the non-local arc radius is defined as a function of crack dimension, a, rather than particle volume.

Due to the non-local arc approach taken, a single value — the arc radius illustrated in Figure 3 — must be defined. Making the non-local arc radius large relative to the incubated crack enables numerical convergence with a relatively coarse mesh, but can provide results that do not capture the localization near the incubated crack front, Figure 4. On the other hand, making the non-local arc radius too small precludes convergence even with a relatively refined mesh. Therefore, an envelope on the non-local domain size must be defined. An analogous argument was previously made by Xue *et al.* for an envelope of non-local volume [21]. Here, the upper bound on the non-local arc radius is defined to be 25% of the crack dimension, a, Figure 3, based on the result that beyond this domain the nucleation metrics are no longer dominated by the presence of the crack. The lower bound of the non-local arc radius was determined by repeatedly refining the mesh and determining the smallest radius from which the non-local nucleation metrics converged. It was found that below a radius of 10% of the crack dimension, a, nucleation metrics did not converge with mesh refinement. This is equivalent to the range used by Gall *et al.* if the crack dimension, a, is substituted for D.

The required mesh refinement for field convergence within the baseline model was investigated within the envelope defined in Figure 4. To determine convergence, nucleation metrics were queried at one-degree intervals along the non-local arc shown in Figure 3. These pointwise values are shown
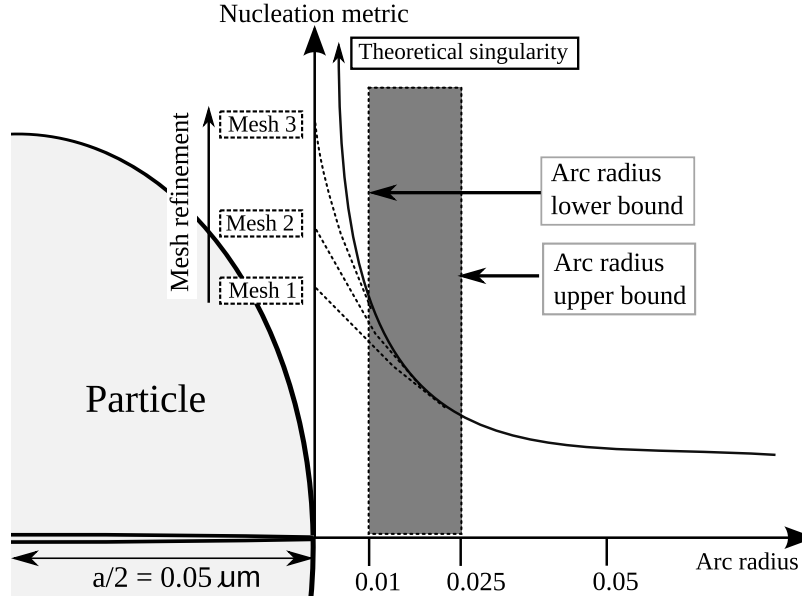
Figure 4. Schematic diagram showing effect of the non-local arc radius on convergence. There is an inherent singularity along the incubated crack front within computed finite element fields.

in Figure 5, where θ corresponds to counter-clockwise movement along the arc. The convergence results for each of the five nucleation metrics and three orientations are too many to be shown here. Therefore, the results for the D_1 nucleation metric from Orientation C are shown. The four levels of mesh refinement were such that element edge lengths in the coarse, medium, fine, and concentrated refinement meshes were 10%, 5%, 1%, and 0.5% of the crack dimension, a, respectively, which correspond to a range of 0.15 to 2.5 million degrees of freedom.

By comparing the nucleation metrics among the four levels of refinement shown in Figure 5, it is seen that results from the fine, and concentrated refinement meshes produce acceptably similar results. In general, the convergence testing revealed that the fine and concentrated mesh refinements were within $\sim 2\%$ at a radius of 25% of the crack dimension, a, and $\sim 5\%$ at a radius of 10% of the crack dimension, a, for the methods given in Equations (8) and (9). Based on these results, it was decided that local element edge lengths of 1% of the observable crack dimension, a, provide sufficiently converged results for arc radii of $\geq 10\%$ of the crack dimension, a, and would be used for the remainder of the baseline simulations. It is important to note here that convergence of the computed finite element fields is also dependent on the grain orientation being modeled as well as the linear and nonlinear iterative solver tolerances. Therefore, it cannot be expected that this refinement level will hold for every possible lattice orientation of the baseline model. It does, however, provide a representative level of refinement.

After analysis of the three analyzed orientations, it was found that the values of all five nucleation metrics are qualitatively similar along the non-local arc within the baseline model, Figure 6. Therefore, further illustration of results is limited to that of the D_1 metric. The following discussion of each set of illustrated results can be taken to be true for each of the nucleation metrics.

(a)

(b)
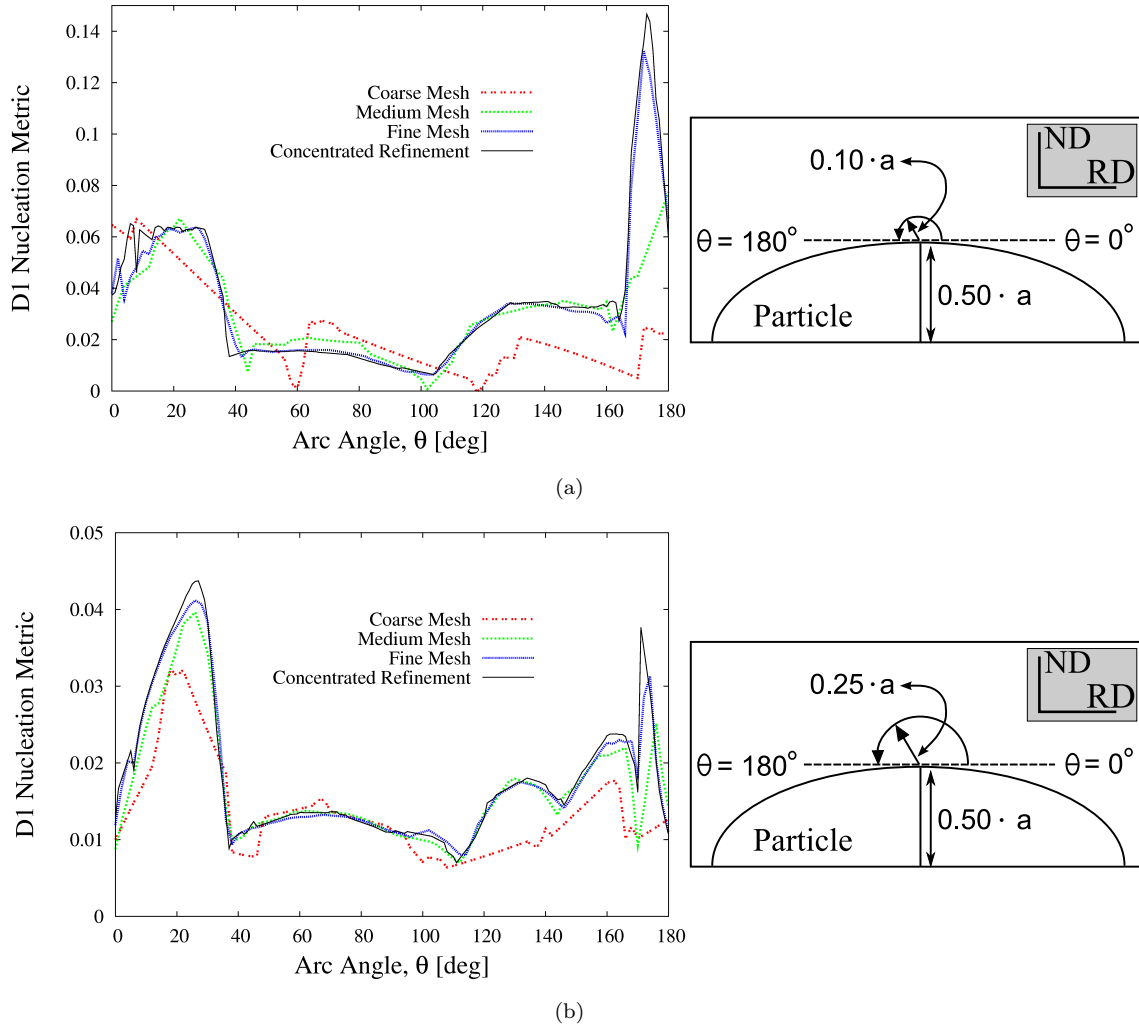
Figure 5. D_1 nucleation metric versus arc angle at four levels of mesh refinement for arc radii equal to (a) 10% and (b) 25% of the crack dimension, a. These results were taken from Orientation C. Note the difference in ordinates.

3.2. Non-local Nucleation Metrics Localization and Accumulation

The effect of orientation on the localization of the nucleation metrics, $D_{1...5}$, can now be studied with the required mesh refinement applied. If the baseline model were simply a cracked hexahedral grain without a relatively stiff surface particle, then it would be expected that the directions of localization would correspond directly to the active slip systems within the grain. However, given the presence of the cracked particle, the directions of localization might not correspond directly with the active slip system directions. Figures 7(a), 7(c), and 7(e) display the D_1 scalar field at
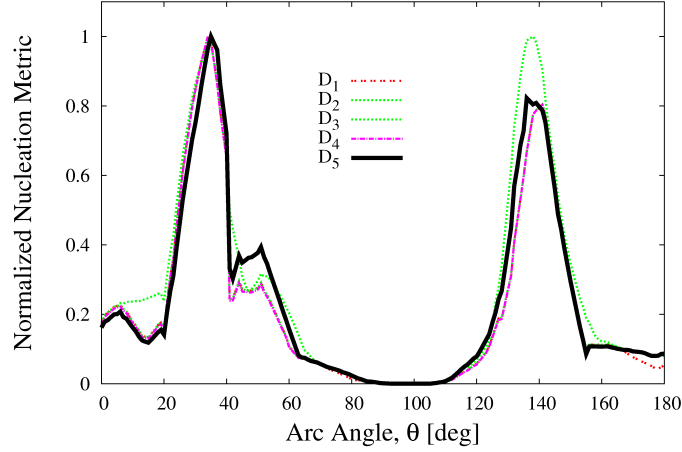
Figure 6. Comparison of $D_{1\ldots5}$ nucleation metrics. Each metric is normalized by its maximum value along the non-local arc. These data were taken from Orientation A with a non-local arc radius of 25% of the crack dimension, a.

the peak of the first load cycle, near the cracked surface particle. Figures 7(b), 7(d), and 7(f) display the directions of the two slip systems with the highest Schmid factor as projected onto the baseline model free surface (an RD-ND plane), which illustrates the correspondence of active slip system directions and nucleation metric localization within the grain. In Figures 7(b), 7(d), and 7(f) the Schmid factor, m, for these systems is given. It is observed that the contours corresponding to localization approximately align with the lattice slip systems with the highest Schmid factors. Also, the Schmid factor corresponds to the distance from the crack front that the localization extends, *i.e.* the higher the Schmid factor, the farther the localization extends away from the crack front.

For the AA 7075-T651 DEN specimen and loading studied in this paper, most of the particles that incubated a crack during cyclic loading did so by the end of the first load cycle; nucleation usually occurred much later in the fatigue life, Figure 2. Therefore, the next step in the baseline study is to investigate the accumulation of the nucleation metrics during cyclic loading and its dependence on grain orientation. Figure 8 displays three plots — one for each grain orientation — of the D_1 metric along the non-local arc with a radius of 25% of the crack dimension, a. By comparing the cyclic accumulation of D_1 among the three orientations considered, Figure 8, it is seen that localization occurs along two specific directions in the RD-ND plane; however, each with varying degrees of localization.

The nucleation metric accumulation is along the same direction at which localization occurred during the first load cycle. There are two angles, θ, that correspond to two distinct peaks in D_1 within Orientation A: about $36°$ and about $140°$, Figure 8(a). These angles are closely aligned with the directions of maximum principle shear stress (in the absence of a particle) for the boundary conditions applied. Similarly, there are two angles that correspond to two distinct peaks in D_1 within Orientation B: about $58°$ and about $152°$, Figure 8(b). There is no accumulation of D_1 after the second load cycle for the peak at $52°$, which is also much less pronounced that the peaks corresponding to Orientation A. Finally, there are two angles that correspond to two distinct peaks in D_1 within Orientation C: about $26°$ and about $154°$, Figure 8(c). Each of these peaks is less
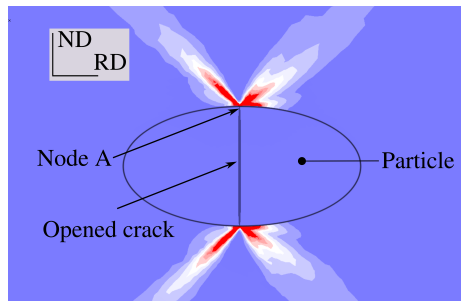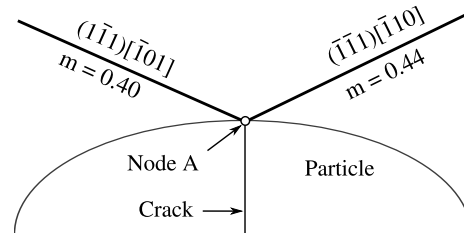
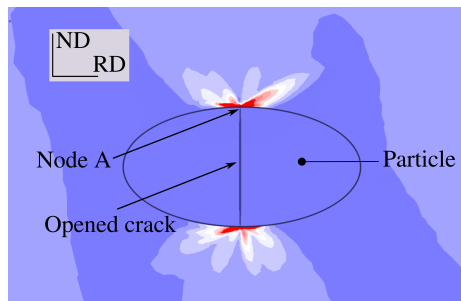(a) D_1 metric color contour for Orientation A
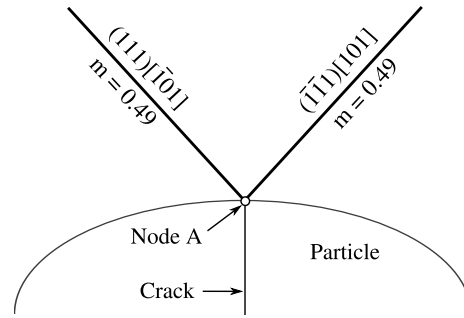
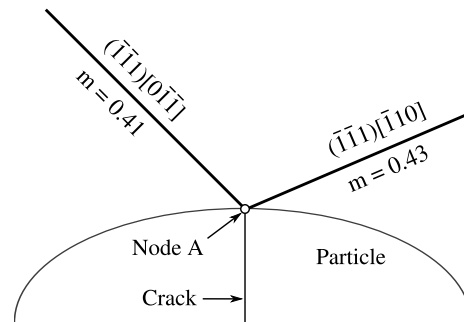(b) Illustration of the 2 slip systems with the highest Schmid factor, m, in Orientation A.
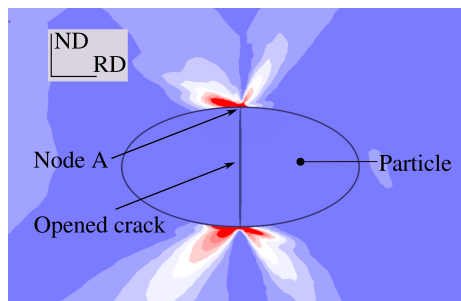
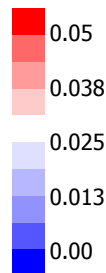(c) D_1 metric color contour for Orientation B

(d) Illustration of the 2 slip systems with the highest Schmid factor, m, in Orientation B

(e) D_1 metric color contour for Orientation C

(f) Illustration of the 2 slip systems with the highest Schmid factor, m, in Orientation C

(g) D_1 metric color contour bar.

Figure 7. Nucleation metric D_1 contour plots at the peak of the first load cycle showing dependence of localization on grain orientation with active systems illustrated.

pronounced than those corresponding to Orientation A. Also from Figure 8(a), D_1 is very nearly zero between the peaks for Orientation A; however, this is not true of Orientations B or C, where damage is more uniformly distributed along the non-local arc. It is apparent that Orientation A induces greater localization than the other orientations simulated. Furthermore, Orientation A localizes and accumulates slip activity in directions aligned with the direction of maximum principle shear stress (in the absence of a particle) and continues to accumulate along those same directions, whereas slip localization is at, or near, the particle-grain interface in Orientations B and C. This provides evidence that the surrounding grain orientation affects the nucleation governing mechanism. Orientation A induces slip localization within the grain, away from the particle-grain interface. Conversely, Orientations B and C induce slip localization along the grain boundary.

3.3. Non-local Nucleation Metrics Regularization

Regularization is used to reduce the spatially-varying nucleation metrics along a non-local arc, *e.g. the data illustrated in Figure 6*, to a single representative value. Two methods for non-local regularization were tested within the baseline study. The first method uses the maximum value of the nucleation metric over all points on the arc,

$$\max D_i\,(r, \theta)\,, \; i = 1\dots 5, \tag{8}$$

where D_i is a nucleation metric and the position on the arc is defined by r and θ. The second approach is based on an average value of the nucleation metric over the arc,

$$\frac{\int_{\theta_1}^{\theta_2} D_i\,(r, \theta)\,d\theta}{\int_{\theta_1}^{\theta_2} d\theta}, \; i = 1\dots 5. \tag{9}$$

The first method, Equation (8), emphasizes nucleation metric localization near the crack front, which corresponds to a specific global direction, θ. The second method, Equation (9), emphasizes the nucleation metric average near the crack front. The bounds of integration on Equation (9), for the baseline study, are such that $\theta_1 = 0$ and $\theta_2 = \pi$. Both methods are used in the baseline model study to quantify the effect of lattice orientation on nucleation. In the next section of this paper, a determination of which method is more physically accurate is made using the replication models.

The regularized non-local nucleation metrics are now calculated from the data illustrated in Figure 8. Tables 2 and 3 summarize the effect of orientation using regularized metrics calculated from the non-local arc with a radius of 25% of the crack dimension, a, at the peak of the fifth load cycle. The five regularized nucleation metrics resulting from Equation (8) are given in Table 2, which correspond to the direction of highest localization.

From Table 2, it is seen that $D_3 = D_2 = D_1$ for Orientations A and C. However, this is not true of Orientation B, in which $D_3 > D_2 = D_1$. Also, values of $D_{1\dots 5}$ in Orientation A tend to be the highest, while those within Orientations C tend to be the lowest. The single outlier in the data is that of D_3 for Orientation B. This result suggests that there is a significant amount of slip activity on a secondary slip plane(s) along the direction of highest localization when the grain is in Orientation B. Therefore, for Orientation B, there are at least two slip planes within the grain that contribute to slip localization. For Orientations A and C, there is a single active slip plane within the grain that dominates slip localization. From these results, it is found that each nucleation metric can vary by approximately 40-60% with variation in grain orientation.

The results of Table 3 differ substantially from those shown in Table 2. Table 3 compares the nucleation metrics obtained by the domain averaging method of Equation (9) among the three
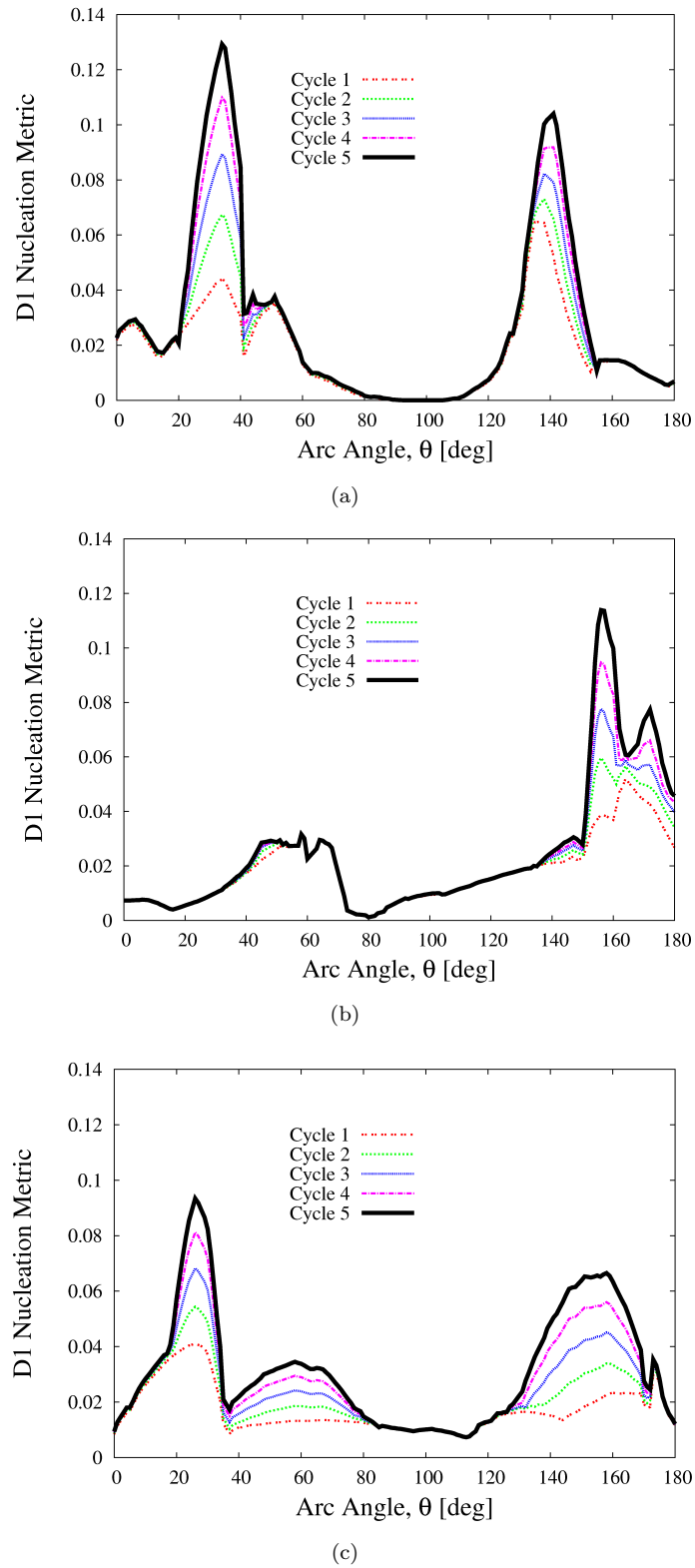
Figure 8. D_1 localization and accumulation along an arc with radius of 25% of crack dimension, a, for the three simulated grain Orientations (a) A (b) B (c) C.

Table 2. Maximum of $D_{1\ldots5}$ nucleation metrics along the arc for orientations A, B, and C at the fifth load peak. The radius of the non-local arc is chosen as 25% of the crack dimension, a.

|	D_1	D_2	D_3	D_4 (MPa)	D_5
Orientation A	0.13	0.13	0.13	29.0	0.19
Orientation B	0.11	0.11	0.15	26.0	0.17
Orientation C	0.09	0.09	0.09	21.0	0.12

Table 3. Average of $D_{1\ldots5}$ nucleation metrics along the arc for orientations A, B, and C at the fifth load peak. The radius of the non-local arc is chosen as 25% of the crack dimension, a.

|	D_1	D_2	D_3	D_4 (MPa)	D_5
Orientation A	0.029	0.029	0.036	6.5	0.045
Orientation B	0.025	0.027	0.034	6.0	0.042
Orientation C	0.032	0.037	0.039	8.2	0.049

orientations simulated. In general, $D_3 \geq D_2 \geq D_1$ for each of the orientations studied, as expected from the definitions given in Section 2. However, unlike the results shown in Table 2, values of $D_{1\ldots5}$ in Orientation C are consistently the highest, while those within Orientation B are consistently the lowest. The reason for this result is illustrated in Figure 8. For Orientation C, Figure 8(c), it is seen that the D_1 metric does not reduce to zero at any point along the non-local arc, and that between the two directions of localization there is a region where D_1 is nearly constant. However, from Figure 8(a), corresponding to Orientation A, the D_1 nucleation metric is zero between the two directions of localization. Lastly, from Figure 8(b), corresponding to Orientation B, there is only one significant direction of localization. Upon integration of these data it is found that, on average, Orientation C induces higher nucleation metrics along the non-local arc, and these are more distributed than in Orientation A. Therefore, it can be concluded that Orientations A and C are fundamentally different in how they induce slip activity. Orientation A induces a more localized slip field, while Orientation C induces a more distributed slip field.

Through five simulated load cycles, the relationship between the regularized non-local nucleation metric and cycle number is found to be nearly linear after the first load cycle for both regularization methods, Figure 9. Figure 9(a) shows that D_1 accumulates at a slightly higher rate for Orientation A than Orientations B and C. However, as expected from the discussion of the results shown in Table 3, Figure 9(b) shows that Orientation C exhibits a larger value of damage than Orientations A or B as the number of cycles increases. The difference among the D_1 accumulation rates for the three orientations is significantly more pronounced in Figure 9(b), which corresponds to the metric averaging method. A fundamental difference between the two methods of non-local regularization is reflected in Figure 9: the averaging method produces relatively high nucleation metrics for distributed plastic slip near the crack, while the maximum method produces relatively high nucleation metrics for localized plastic slip.

It is evident from this study of computed $D_{1\ldots5}$ scalar fields and their accumulation, that orientation strongly influences the likelihood of crack nucleation from a cracked second-phase particle, for the three orientations considered. Therefore, one would expect that there exists a 'worst-case' grain orientation surrounding a cracked second-phase particle. As illustrated in Figure 9(a), Orientation A is among the 'worst-case' set of orientations from its relatively pronounced localization of the nucleation metrics. It is important to note that Orientation A is among the twisted-cube orientations, observed by Patton to be likely sites of crack nucleation. Therefore, there is consistency between the baseline study results computed using the non-local maximum
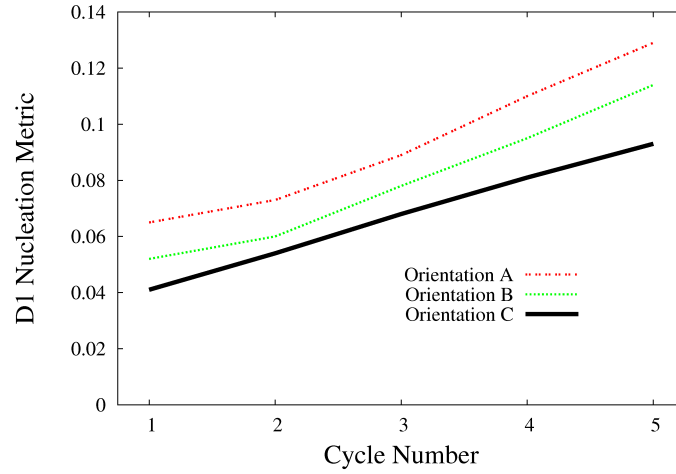
(a)
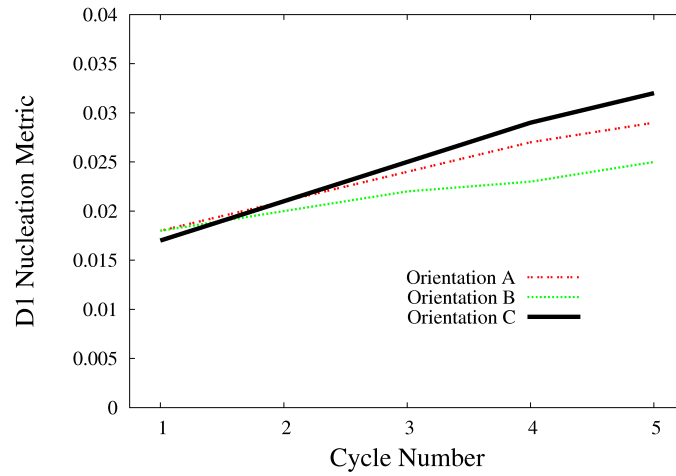
(b)

Figure 9. Accumulation behavior of D_1 nucleation metric over five simulated load cycles. (a) Metrics computed using Equation (8) (b) Metrics computed using Equation (9). Note the difference in ordinates.

approach, Equation (8), and the experimental findings of Patton *et al.* [10].

From this baseline study, it is not possible to distinguish which method of non-local regularization is most valid, although characteristics of each have been revealed. In the next section, information gained from the baseline model is applied to the simulation of realistic polycrystal models to test the validity of the five proposed non-local nucleation metrics, Equations (3)-(7), and two non-local regularization methods, Equations (8) and (9).

4. Replication Models

The nucleation metrics and non-local regularization methods are now used to study the nucleation phase of two cracked second-phase particles, which were observed to incubate a fatigue crack during fatigue loading of the DEN specimen. These two particles are interesting to compare because both particles had cracked by the end of first loading cycle; the particle in Figure 10(a), Particle #50 (P50), was cracked before load application and the particle in Figure 11(a), Particle #135 (P135), cracked at 80% of the first load peak. However, P50 nucleated a crack into the surrounding grains from the top part of the cracked particle in Figure 10 at about 30 cycles of loading and from the lower part of the cracked particle between 1000 and 3000 load cycles (observations were not made between cycles 1000 and 3000). In contrast, P135 had not nucleated a crack into the surrounding grain by 3000 cycles of loading.

Given that both of these particles were separated by only a fraction of a millimeter, on the free surface of the same notch of the DEN specimen, the key question is: Why did P50 nucleate a crack while P135 did not? This section attempts to answer this key question using the replication models, the polycrystal elastic-viscoplastic constitutive model, and nucleation metrics defined in Section 2.

### 4.1. Finite Element Model Generation and Fatigue Simulation

Finite element models that directly replicate the observed microstructures, local to P50 and P135, were generated to test the validity of the non-local regularization methods and nucleation metrics. The microstructures, local to P50 and P135, are illustrated in Figures 10 and 11; the experimental observations are shown in Figures 10(a) and 11(a) and the corresponding replicated finite element models are shown in Figures 10(b) and 11(b). The coloring in these two figures corresponds to the grain orientation as measured by EBSD. Slight differences between the particle geometries obtained from secondary electron images, illustrated in the expanded portions of Figures 10(a) and 11(a), and the particle geometries obtained from EBSD, illustrated in the expanded portions of Figures 10(b) and 11(b), exist because the secondary electron images reflect the particle geometry on the specimen surface, while EBSD provides measurements of the microstructures slightly below the observed surface.

The finite element models, Figures 10(b) and 11(b), were generated by first tracing the grain boundaries given by EBSD within the notch of an AA 7075-T651 DEN specimen. The portion of the image that is expanded in Figures 10(b) and 11(b) shows the employed finite element mesh within each cracked particle. Each enclosed region was associated with the observed lattice orientation, unless the region was a particle, in which case the region was defined as linear elastic and isotropic. An automated process was developed to import individual region geometry and corresponding orientations into ABAQUS$^{\circledR}$ through a Python scripting interface, where construction of the 3-D polycrystal, meshing, and application of material parameters and boundary conditions were completed. This overall process — from microscopy to 3-D finite element model — quickly generated the replication models, and after the grain boundaries were traced, each meshed model took approximately two minutes to generate. A crack was then inserted in the target particle and only the grains affected by the change in geometry were remeshed. Analysis was then performed using an in-house parallel finite element solver.

Since no morphology information was acquired in the TD, the traced grain boundaries were extruded 74 μm in the TD to be consistent with the experimentally observed grain aspect ratios. Similarly, the traced particle boundaries were extruded 3 μm in the TD. Displacement boundary
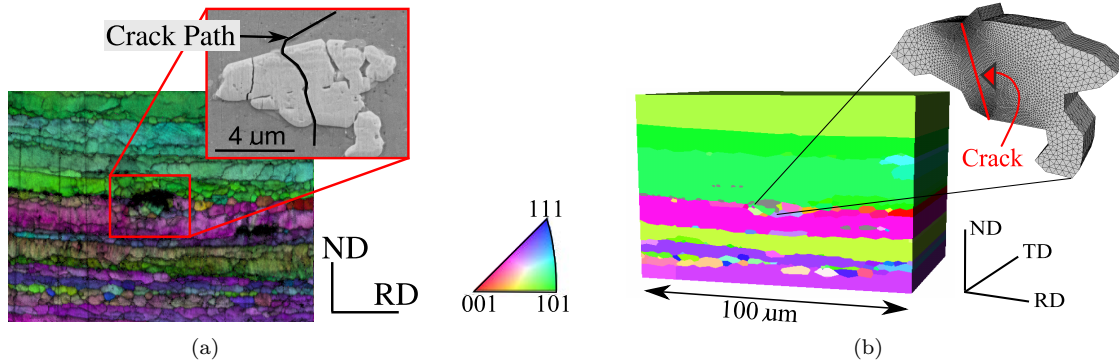
Figure 10. The P50 2.5-D finite element model, generated from experimental data, shown with inverse pole figure [100] color contour map. (a) Inverse pole figure with detail of Al_7Cu_2Fe particle region. (b) Corresponding finite element model with zoom on meshed, cracked particle.
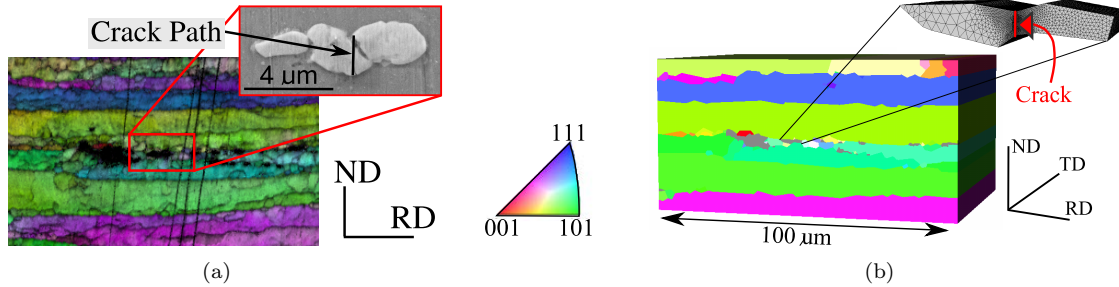
Figure 11. The P135 2.5-D finite element model, generated from experimental data, shown with inverse pole figure [100] color contour map. (a) Inverse pole figure with detail of Al_7Cu_2Fe particle region. (b) Corresponding finite element model with zoom on meshed, cracked particle.

conditions were applied to produce a local strain field equal to that measured within the DEN notch during experiment, as discussed in Section 3. The P50 model contains 102 grains and 16 particles, and the P135 model contains 60 grains and 12 particles. Both have approximately 1 million quadratic tetrahedral elements ($\sim$4.5 million degrees of freedom) and are 100 μm long in the RD, much larger than the particle dimensions, to minimize any boundary effects near the crack front.

It was shown in Section 3 that a non-local arc radius of 10–25% of the observable crack dimension, a, was reasonable and provides reliable results, if the mesh is sufficiently refined. The two replication models were meshed such that the hybrid quadratic tetrahedra, near the crack front, had element edge lengths of $\sim$1% of the crack dimension, a. It was also concluded from the baseline study that relatively few load cycles were necessary, since after the first load cycle the $D_{1\ldots5}$ accumulation is nearly linear. Although the simulation of 10 or even 100 cycles using the finite element models developed here is tractable, it might be unduly time consuming and unnecessary given the nearly linear nucleation metrics accumulation rates. Therefore, five cycles of loading

were simulated and $D_{1...5}$ were linearly projected to the desired number of cycles for comparison of results.

4.2. Non-local Nucleation Metric Localization and Accumulation

The illustrated results focus on the D_1 nucleation metric, for the sake of brevity. Like the baseline models, it was observed here that the nucleation metrics were qualitatively similar. Also, it is assumed here that nucleation is enabled by slip that is localized in the crystal lattice near the crack front. It was noted that the presence of the cracked particle in the baseline models influences the directions of localization and, therefore, slip system directions may not correspond exactly with the global contours of localized nucleation metrics. This particle effect is exacerbated for the replication models. In addition to a stiff second-phase particle — now irregularly shaped — there are grain boundaries and additional second-phase particles throughout the models. Therefore, it is expected that localization will react not only to active lattice slip systems, but also to the modeled microstructural heterogeneities, *e.g.* grain, subgrain, and particle-grain boundaries.

Figures 12(a) and 12(c) display the D_1 nucleation metric field near each replicated particle at the first load peak. Comparing Figures 12(a) and 12(c) with Figures 12(b) and 12(d), respectively, illustrates the correspondence of active slip systems and heterogeneities with localization in the grains surrounding each replicated particle. It is observed that the contours corresponding to slip localization align with either active lattice slip systems or particle-grain interfaces. In several cases, the direction corresponding to an active slip system intersects with adjacent particle geometry, precluding the possibility of crack growth in that direction. In the case of Node 436 in the P135 model, the microstructure at the crack front includes multiple grains, further complicating the MSFC growth process. As with the baseline models, it is seen that a higher Schmid factor, m, intensifies localization.

Figures 13 and 14 display the computed D_1 metric along the non-local arc with a radius of 25% of the crack dimension, a, at each crack front node on the free surface. It is seen that localization occurs along two directions at each of the crack front free-surface nodes. In particular, the accumulation is constrained to the directions along which localization occurred during the first load cycle, as was observed in the baseline models. However, as expected, the direction of localization and accumulation does not always correspond exactly to the active slip system direction(s) illustrated in Figure 12.

At Node 511 in P50, where nucleation first occurred, the D_1 metric is dominated by the particle-grain interface, which corresponds to $\theta \approx 50°$ in Figure 13(b). At the other side of the P50 particle, Node 517, the resulting non-local metrics are similar to those of Orientation A in the baseline models: the active slip-systems align with the contours along which D_1 is localized and accumulated, and these correspond with the directions of maximum principle shear, Figure 13(c). By comparing the cyclic accumulation of metric D_1 within P135, Figure 14, at the two free-surface crack front nodes, it is seen that localization occurs along two directions in both cases. Accumulation is constrained to the particle-grain interface at both of these crack front nodes in P135.

4.3. Non-local Nucleation Metrics Regularization

The regularized nucleation metrics are now calculated from the data illustrated in Figures 13 and 14. The five nucleation metrics resulting from Equation (8), presented in Table 4, correspond to the direction of highest localization. First, $D_3 \geq D_2 \geq D_1$, as expected from the discussion and
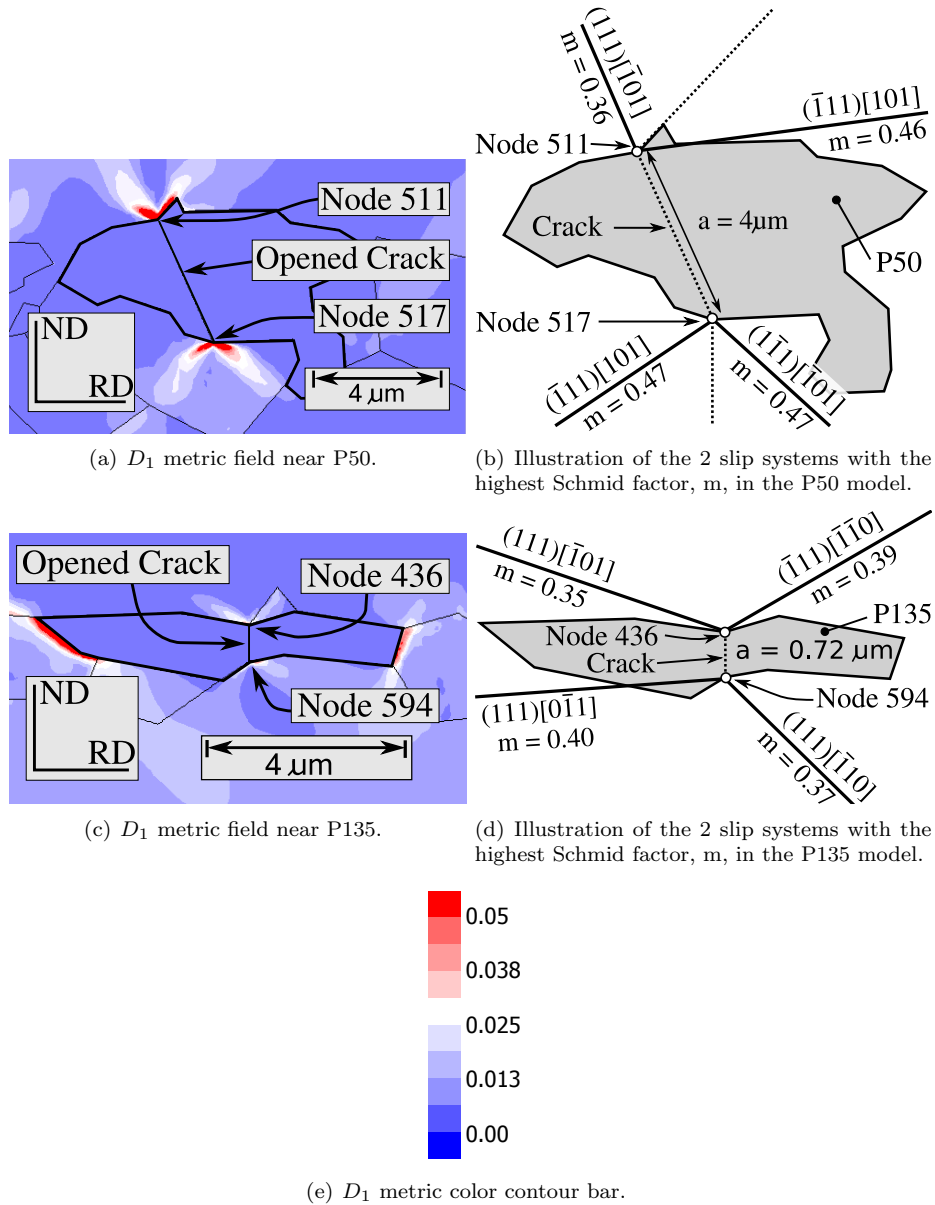
(a) D_1 metric field near P50.

(b) Illustration of the 2 slip systems with the highest Schmid factor, m, in the P50 model.

(c) D_1 metric field near P135.

(d) Illustration of the 2 slip systems with the highest Schmid factor, m, in the P135 model.

(e) D_1 metric color contour bar.
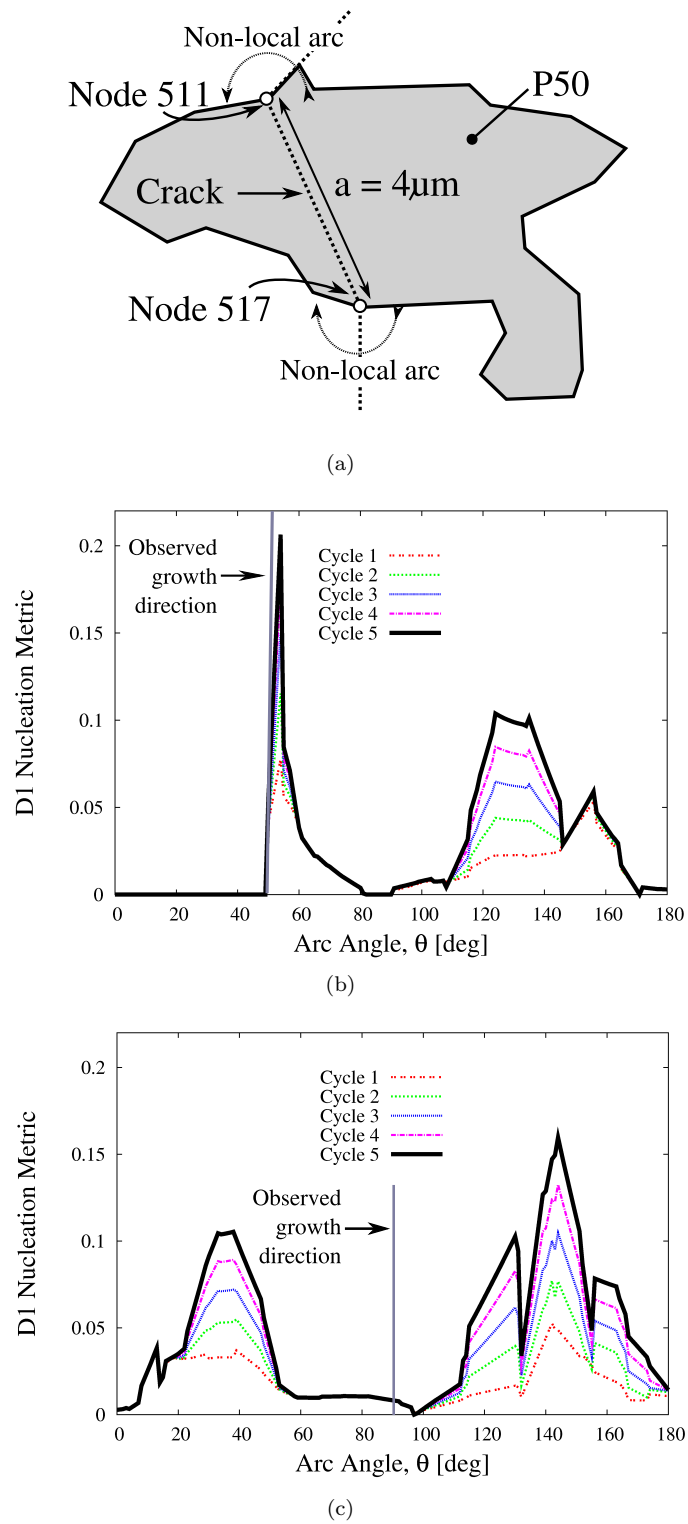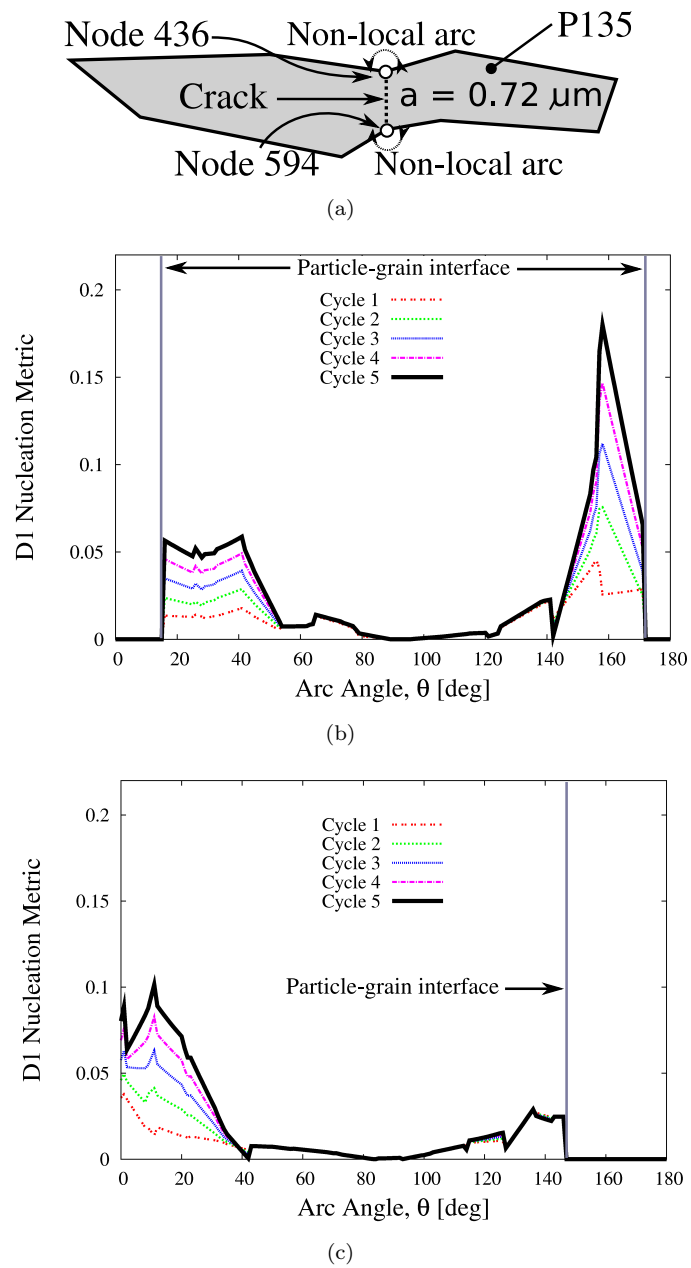
Figure 12. Comparison of (a) P50 and (b) P135 D_1 fields at first peak load.

(a)

(b)

(c)

Figure 13. Accumulation of the D_1 metric within the P50 model at both crack front points that intersect the free surface, (a) P50 outline showing the non-local arc (b) Node 511 (c) Node 517 These data were extracted along a non-local arc with a radius of 25% of the crack dimension, a, 1.0 μm.

(a)

(b)

(c)

Figure 14. Accumulation of the D_1 metric within the P135 model at both crack front points that intersect the free surface, (a) P135 outline showing the non-local arc (b) Node 436 (c) Node 594. These data were extracted along a non-local arc with a radius of 25% of the crack dimension, a, 0.18 μm.

definitions given in Section 2. Considering P50, it is seen that $D_3 > D_2 = D_1$. This result affirms that there is a significant amount of slip activity on secondary slip system(s) along the direction of highest localization. Furthermore, the additional active system(s) are not on the most active slip plane; this follows directly from the definitions of $D_{1,2,3}$. Therefore, for P50, there are at least two slip planes within the neighboring grains that contribute to slip localization along the direction of maximum localization. For P135, this is not the case, since $D_3 = D_2 \approx D_1$. Therefore, for P135, there is a single active slip plane within the neighboring grains that contributes to slip localization.

We restrict direct comparison of the nucleation metric values presented for P50 and P135 to points where the nucleation mechanism is consistent, *i.e.* slip localization is along the particle-grain interface or within the surrounding grain. Therefore, the regularized non-local nucleation metrics near Node 511 in P50 can be compared to Nodes 436 and 594 in P135; Node 517 in P50 is a unique case that cannot be directly compared with other results. From Table 4, it is seen that the regularized $D_{1...4}$ are higher near Node 511 in P50 than for Nodes 436 and 594 in P135. This result is in agreement with the experimental observation that P50 nucleated a crack from Node 511, while P135 did not. However, the regularized value for D_5 at Node 511 in P50 is lower than that of Node 436 in P135, which is not in agreement with experimental observation.

Fundamentally, the results shown in Tables 4 and 5 are significantly different, where Table 5 gives the nucleation metric average of the data shown in Figures 13 and 14. For the replication models, the domain of integration of Equation (9) corresponds to the portion of the non-local arc that was within a grain, *i.e.* if a portion of the non-local arc was within a particle region then that portion was neglected during integration. In Table 5, it is seen that $D_3 \geq D_2 \geq D_1$ for P50 and P135, as expected. Also, the regularized $D_{1...5}$ are higher near Node 511 in P50 than for Nodes 436 and 594 in P135. This result is in agreement with the experimental observation that P50 nucleated a crack from Node 511, while P135 did not.

Determination of slip activity on secondary slip systems can be made by comparing among the regularized $D_{1,2,3}$ metrics. Overall, the five nucleation metrics tend to be significantly larger for P50 than P135 along the non-local arc when using either non-local regularization method. Therefore, it is concluded that using either non-local regularization method, along with any of $D_{1...5}$, predicts that P50 is more likely to nucleate a crack, which is in agreement with experimental observations. However, this conclusion is based on the nucleation metric values after only 5 cycles, while the actual nucleation event was observed to occur later in the fatigue life.

Table 4. Maximum $D_{1...5}$ nucleation metrics along the arc for P50 and P135 at the peak of the fifth load cycle. Two values are given, one for each point where the crack meets the matrix material on the free surface. These data were extracted along a non-local arc with a radius of 25% of the crack dimension, a, (1.0 μm for P50 and 0.18 μm for P135).

		D_1	D_2	D_3	D_4 (MPa)	D_5
P50	Node 511	0.20	0.20	0.25	46.0	0.24
	Node 517	0.16	0.16	0.20	37.0	0.21
P135	Node 436	0.18	0.18	0.18	40.0	0.29
	Node 594	0.10	0.11	0.11	24.0	0.13

4.4. Comparison of the Projected Regularized Nucleation Metrics to Experimental Observations

The nucleation metric D_1 is again used as a basis for discussion to illustrate direct comparison with the experimental observations. As was observed in the analysis of the baseline model, the relationships between the nucleation metrics and cycle number were found to be linear through

Table 5. Average of $D_{1...5}$ nucleation metrics along the arc for P50 and P135 at the peak of the fifth load cycle. Two values are given, one for each point where the crack meets the matrix material on the free surface. These data were extracted along a non-local arc with a radius of 25% of the crack dimension, a, (1.0 μm for P50 and 0.18 μm for P135).

		D_1	D_2	D_3	D_4 (MPa)	D_5
P50	Node 511	0.038	0.041	0.044	9.0	0.052
	Node 517	0.047	0.050	0.060	11.0	0.064
P135	Node 436	0.032	0.032	0.037	7.1	0.049
	Node 594	0.022	0.025	0.028	5.6	0.033

five simulated load cycles, after the first load cycle peak, for both non-local regularization methods, Figures 15 and 16. This linear relationship allows for a first-order projection of damage accumulation to larger numbers of cycles. At Node 511 in P50, where nucleation initially occurred, the regularized non-local metrics were linearly projected to 30 cycles. For P135, where nucleation did not occur by 3000 load cycles, the non-local metrics were linearly projected 30 cycles for comparison with Node 511 in P50.

The projected nucleation metrics, regularized using Equation (8), are shown in Figures 15(a) and 16(a). The regularized D_1 metric is projected to be 0.96 at Node 511 in P50 at 30 load cycles. For P135 at 30 cycles, the regularized D_1 metric values are 1.04 and 0.50 at nodes 436 and 594, respectively. Thus a slightly larger value of D_1 is computed for P135, Node 436, from which nucleation was not observed to occur. The projected nucleation metrics, regularized using Equation (9), are shown in Figures 15 and 16. The regularized non-local D_1 metric at Node 511 in P50 at 30 load cycles is projected to be 0.15. For P135 the corresponding D_1 metric has values 0.15 and 0.09 at Nodes 436 and 594, respectively. Therefore, after the linear projection of the regularized non-local nucleation metrics, neither regularization method is in agreement with experimental observations since the regularized D_1 metric at Node 436 in P135 is greater than or equal to that of Node 511 in P50.

After completing this study, it is evident that the geometric modeling strategy, in conjunction with the assertions of linear projection and a direct scaling of the non-local arc with the crack dimension, a, are insufficient to capture the complete material response. The projection of microstructure observed at the free surface into the TD, for example, limits the predictive capability of the models. Furthermore, it is likely that the slip localization surrounding the incubated cracks in P50 and P135 begin to saturate after an unknown number of load cycles, which is not captured in the linear projection of the regularized non-local metrics. The value of the D_1 metric for Node 511 in P50 was found to be an order of magnitude higher than either of the nodes in P135 after repeating these linear projections with the non-local arc radius defined as 1 μm for both P50 and P135. The assertions of linear projection and direct scaling of the non-local arc with the crack dimension, a, are the subject of a continued study. It is also possible that nucleation occurred along the particle-grain interface near Node 436 in P135, but never extended into the surrounding grain, as was seen near Node 511 in P50, and therefore was not observed.

The nucleation event from P50 at Node 517 is unique in this study since it is the only instance where the highest initial metric value and subsequent accumulation were not along a particle-grain interface. The regularized non-local metrics were linearly projected 1000 and 3000 cycles to provide a range of the regularized metric values which correspond to the observed number of cycles required for nucleation. Projecting the regularized D_1 metrics given by Equation (8) results in a range of 27.5–82.5. Projecting the regularized D_1 metrics given by Equation (9) results in a range of 7.3–

21.9. These regularized metrics, which correspond to the observed range of nucleation, are about an order of magnitude higher that those corresponding to slip localization along the particle-grain interface, indicating a strong influence of microstructural features on MSFC growth.

Any localized variations in the underlying mechanisms associated with crack nucleation will result in, at a minimum, variations in threshold nucleation metric values. For example, a low fracture energy associated with a particle-grain interface is expected to play an important role in the nucleation event. Slip localization occurring along the direction of a particle-grain interface may lead to more rapid crack nucleation than similar levels of slip localization directed away from a particle-grain interface. A needed enhancement to the non-local approaches presented here is the introduction of threshold variations of the non-local metrics to account for such variations in the governing nucleation mechanisms. The non-local maximum approach, Equation (8), is well suited for such a modification because it is associated with a localization direction for which a specific threshold value can be computed using the replication modeling procedure presented here. The investigation of additional nucleation metrics and threshold values particular to microstructural heterogeneities is planned for future studies.

### 4.5. Concluding Remarks on the Replication Models

The dotted line extending from Node 517 in P50, in Figure 12(b), shows the observed crack nucleation direction. Recalling the qualitative results of the baseline study, the localization and accumulation of metric D_1 near Node 517 in P50 are occurring along a similar direction to that computed for Orientation A of the baseline model. It is noted that the grain that borders P50 and contains Node 517 has a twisted-cube orientation which was mentioned previously to be a likely site of crack nucleation [10].

By observing the D_1 metric contour field near Node 517 of the P50 model, Figure 12(a), and the corresponding values along the non-local arc, Figure 13(c), it is apparent that the slip field is symmetric with respect to the crack plane. It is reasoned here that the symmetry of localization about the crack plane, which seems to be characteristic of the twisted-cube lattice orientation, acts to blunt the crack front, and subsequently, the crack nucleates and propagates in an apparent Stage II manner, *i.e.* crack growth does not coincide with a crystallographic plane. Laird presented a similar argument based on several experiments investigating single and polycrystalline metallics [13]. Laird asserted that both Stage I and II fatigue crack propagation occur by plastic blunting of the crack front. This assertion was based on observations of Stage II propagation and an assumption that both stages were dominated by the same mechanism, slip localization, since Stage I propagation was then difficult to observe directly [13]. Direct observation of the plastic blunting process revealed that, upon propagation, a crack plane would bisect two dominant slip systems acting in symmetry about the crack plane [13].

Laird also conjectured that, in a polycrystalline material, the presence of microstructural heterogeneities would tend to enforce an asymmetry about the crack plane [13]. It has been shown in this section that even in the presence of a relatively stiff inclusion certain orientations may enforce symmetry of slip localization with respect to the crack plane. On the other hand, it has also been shown that local microstructural geometry can enforce a dominant asymmetry with respect to the crack plane. This asymmetry can occur in the cases of a subgrain or particle-grain interface, or, as noted by Laird, in cases of slip systems orientated at "inconvenient" angles to the crack plane [13]. It is important to note here that if the grain material is represented using an isotropic elastic-plastic model, this concurrence of grain orientation and microstructural geometry local to the crack can
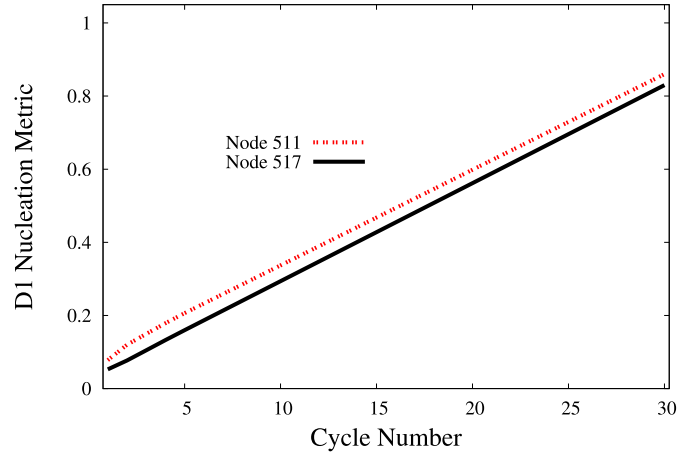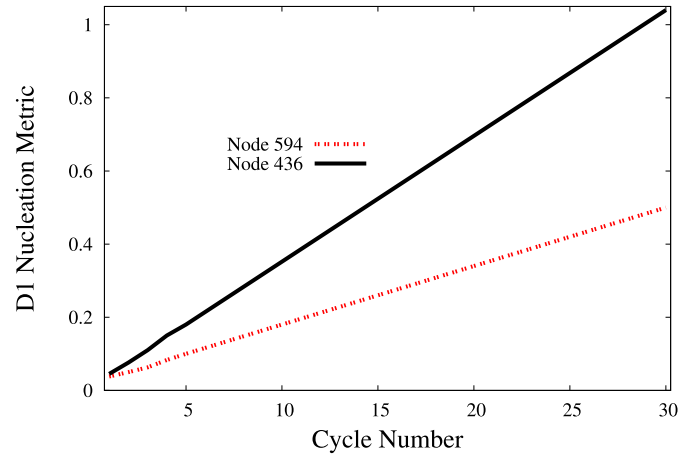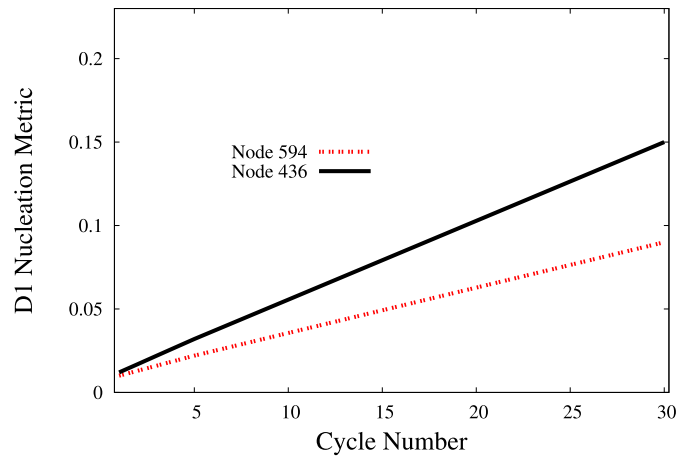
(a)
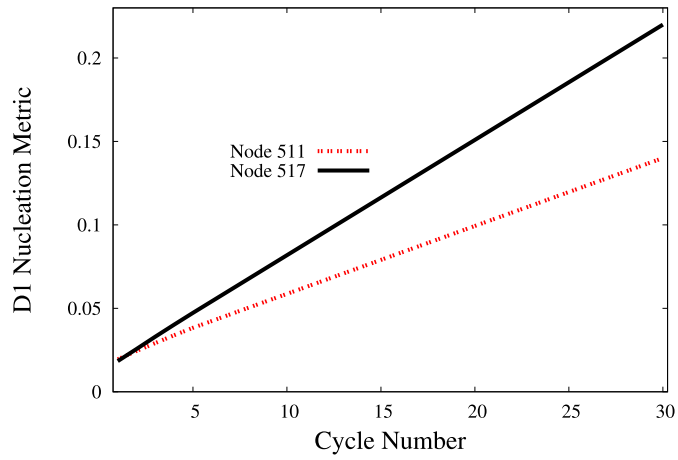
(b)

Figure 15. P50 non-local nucleation metric, D_1, accumulation over five cycles of simulated loading, linearly projected to 30 cycles. (a) non-local maximum method. (b) non-local averaging method. Note the difference in ordinates.

not be represented.

It is asserted here that the maximum non-local approach, Equation (8), is beneficial because it is better suited to capture the local behavior that governs crack nucleation. The maximum non-local method may also be used as a criterion for directionality of crack nucleation and propagation during MSFC growth simulation. If localization is highly asymmetric due to either a microstructural heterogeneity or slip system activity, then Stage I behavior is expected and the corresponding direction can be taken as the direction of propagation at a crack growth step. Conversely, if localization is symmetric about the crack plane, Stage II behavior is expected and the direction

(a)

(b)

Figure 16. P135 non-local nucleation metric, D_1, accumulation over five cycles of simulated loading, linearly projected to 30 cycles. (a) non-local maximum method. (b) non-local averaging method. Note the difference in ordinates.

which bisects the symmetry could be taken as the direction of propagation. Furthermore, the antecedents of high-localization, *e.g.* subgrain boundaries, particle-grain interfaces, or active slip-systems, must be combined with a corresponding nucleation metric threshold to predict nucleation on a case-by-case basis.

5. Summary and Conclusions

The objective of this paper, the second in a series, is to further develop a framework for computationally simulating MSFC growth in AA 7075-T651. This paper focused on crack nucleation from second-phase particles in this alloy. It was hypothesized that the nucleation stage of MSFC growth can be predicted by computing a non-local nucleation metric near the front of a crack through a particle. This hypothesis was tested by employing a combination of experimentation and finite element modeling in which five nucleation metrics and two non-local regularization methods were tested for validity. Initially, a baseline model was studied to illustrate the dependence of each of the nucleation metrics on orientation, number of cycles, and non-local regularization methods. The baseline model study provided five qualitative insights:

(i) Orientation A induces $D_{1...5}$ driven localization near the crack front to a greater degree than the other two orientations tested.

(ii) Orientation C induces a relatively widespread $D_{1...5}$ field near the crack front.

(iii) The calculation of $D_{1...5}$ accumulation rate is dependent on the employed non-local regularization procedure.

(iv) The baseline model is in qualitative agreement with experimental observations that orientations of the twisted-cube type appear to induce crack nucleation.

(v) The accumulation of nucleation metrics, $D_{1...5}$, using either non-local calculation method, is nearly linear after the first load cycle, so metrics $D_{1...5}$ can be projected through; however, further investigation into the validity of this linear projection is needed.

The results of this study were then initially validated against microstructural models constructed directly from experimental data. Compute clusters and state-of-practice experimental technologies provided the capability for preliminary validation simulation of physical mechanisms at work during the crack nucleation stage of the MSFC phase. The results of this study were used to determine the validity of using a continuum crystal plasticity model and a non-local nucleation metric to predict the nucleation event. After five cycles of simulated fatigue loading, which were projected to 30 cycles, four key items were uncovered:

(i) The antecedent of localization, *e.g.* subgrain boundary, particle-grain interface, or active slip-system in twisted-cube lattice, must be combined with a corresponding nucleation metric threshold to predict nucleation on a case-by-case basis.

(ii) The method of non-local regularization has important implications on the outcome of the prediction of nucleation, since each inherently emphasizes certain mechanisms.

(iii) After five load cycles, the replication models show the same linear accumulation of $D_{1...5}$ — similar to that of the baseline models.

(iv) Stage II propagation was observed to occur in the presence of a symmetrical slip field with respect to the crack plane, which is consistent with the concept of plastic blunting [13, 41].

The elastic-viscoplastic polycrystal constitutive model employed here does not inherently capture size effect. Therefore, the effect of particle crack size was not captured in this study. Defining a physically-justifiable non-local arc size, one that does not scale directly with particle crack size, would effectively incorporate size effect into the nucleation metric values. However, it is not known what fixed size of non-local arc is physically justifiable. Therefore, the non-local arc

radius was defined as a fraction of the observable particle crack dimension, *a*, and this approach precludes identification of any nucleation metrics that are size dependent.

The elastic-viscoplastic polycrystal model is capable of simulating slip on individual slip-systems which, although in a smeared fashion, enables the simulation of slip localization and accumulation during cyclic loading. This simulation capability enables qualitative insight into two important questions raised from experimental observation: 1) Do cracks nucleate in Stage I or Stage II for this particular alloy, and why?, and 2) To what extent does grain orientation dictate where and when incubated cracks nucleate? Stage I crack growth was not observed to occur in the models studied here, which is in agreement with the experimental observations made by Gupta [18]. Crack nucleation was observed herein to occurr along a particle-grain interface, in one case, and in Stage II in another case. Also, it is evident that slip localization symmetry is a driving force for Stage II. It was also found that grain orientation plays a fundamental role in the crack nucleation mechanism. Furthermore, there is qualitative consistency among the baseline models, replication models, and past experimental observations, which all suggest that a set of particular grain orientations are most likely to nucleate fatigue cracks. However, it still unknown whether the apparent Stage II nucleation and propagation is driven by Mode I behavior, the availability of relatively low-energy sub-grain boundaries, or by the uptake of hydrogen, or some combination thereof, as suggested by Gupta [18]. Tangential stress along the non-local arc will be added to the presented slip-based nucleation metrics in future computational modeling studies to investigate the possibility of Mode-I behavior.

A complete understanding of the physical response and necessary statistics of the microstructure during MSFC propagation, in each stage and proper sequence, is needed to model the MSFC phase in its entirety. Further simulation is necessary to completely validate qualitative and quantitative models for the prediction of the incubation and nucleation stages of MSFC growth. The next paper in this series will be dedicated to further investigation of the validity of the non-local nucleation metrics and calculation methods presented here on a number of additional replication models. This calibration will enable the identification of particles that will nucleate a crack, rather than the identification of particles that induce a relatively high localization, as was done here. In addition, replication models will be compared against experimental data to further calibrate and validate the incubation simulation methodology presented in the first paper of this series [1].

Acknowledgments

References

[1] J. E. Bozek, J. D. Hochhalter, M. G. Veilleux, M. Liu, G. Heber, S. D. Sintay, A. D. Rollett, D. J. Littlewood, A. M. Maniatty, H. Weiland, R. J. Christ Jr, J. Payne, G. Welsh, D. G. Harlow, P. A. Wawrzynek, and A. R. Ingraffea. A geometric approach to modeling microstructurally small fatigue crack formation: I. Probabilistic

simulation of constituent particle cracking in AA 7075-t651. *Modelling and Simulation in Materials Science and Engineering*, 16(6):065007 (28pp), 2008.

[2] L. Christodoulou and J. Larsen. Using materials prognosis to maximize the utilization potential of complex mechanical systems. *JOM*, 56:15–19(5), March 2004.

[3] J. R. Brockenbrough, A. J. Hinkle, P. E. Magnusen, and R. J. Bucci. Microstructurally based model of fatigue and growth. In C.E. Harris, editor, *Proceedings, FAA/NASA International Symposium on Advanced Structural Integrity Methods for Airframe Durability and Damage Tolerance*, volume NASA Conference Publication 3274, Part I, pages 71–84, September 1994.

[4] J. Fan, D. L. McDowell, M. F. Horstemeyer, and K. Gall. Computational micromechanics analysis of cyclic crack-tip behavior for microstructurally small cracks in dual-phase Al-Si alloys. *Engineering Fracture Mechanics*, 68:1687–1706, October 2001.

[5] S. Suresh. *Fatigue of Materials*. Cambridge University Press, Cambridge, 1998.

[6] J. Payne, G. Welsh, R.J. Christ, J. Nardiello, and J. Papazian. Observations of fatigue crack initiation in 7075-t651. *International Journal of Fatigue*, Accepted Manuscript, 2009.

[7] Y. Murakami and M. Endo. Effects of defects, inclusions and inhomogeneities on fatigue strength. *International Journal of Fatigue*, 16:163–182, Apr 1994.

[8] D. Taylor. On the use of P-a plots to model the behaviour of short fatigue cracks. *International Journal of Fatigue*, 14:163–168, May 1992.

[9] C. J. Taylor, T. Zhai, A. J. Wilkinson, and J. W. Martin. Influence of grain orientations on the initiation of fatigue damage in an Al-Li alloy. *Journal of Microscopy*, 195(3):239–247, Sep 1999.

[10] G. Patton, C. Rinaldi, Y. Brechet, G. Lormand, and R. Fougeres. Study of fatigue damage in 7010 aluminum alloy. *Materials Science and Engineering: A*, 254:207–218(12), 15 October 1998.

[11] Y. Xue, H. El Kadiri, M. F. Horstemeyer, J. B. Jordon, and H. Weiland. Micromechanisms of multistage fatigue crack growth in a high-strength aluminum alloy. *Acta Materialia*, 55(6):1975–1984, 2007.

[12] C. Q. Bowles and J. Schijve. The role of inclusions in fatigue crack initiation in an aluminum alloy. *International Journal of Fracture*, 9(2):171–179, 06/01 1973.

[13] C. Laird. *The influence of metallurgical structure on the mechanisms of fatigue crack propagation*, volume ASTM STP 415, pages 131–167. Am. Soc. Testing Mats., 1967.

[14] David L. McDowell. Simulation-based strategies for microstructure-sensitive fatigue modeling. *Materials Science and Engineering A*, 468-470:4–14. 15 Nov, 2007. Special Issue: The McEvily Symposium: Fatigue and Fracture of Traditional and Advanced Materials, TMS 2006; ML: A356; Ti-6Al-4V.

[15] W. L. Morris and M. R. James. Statistical aspects of fatigue crack nucleation from particles. *Metallurgical Transactions*, 11A:850–851, 1980.

[16] H. Weiland, J. Nardiello, S. Zaefferer, S. Cheong, J. Papazian, and D. Raabe. Microstructural aspects of crack nucleation during cyclic loading of AA7075-T651. *Engineering Fracture Mechanics*, In Press, Corrected Proof:–, 2008.

[17] M. Oja, K.S. R. Chandran, and R.G. Tryon. Orientation imaging microscopy of fatigue crack formation in waspaloy: Crystallographic conditions for crack nucleation. *International Journal of Fatigue*, In Press, Accepted Manuscript:–, 2009.

[18] V. K. Gupta. *Diffraction-based study of fatigue crack initiation and propagation in aerospace aluminum alloys*. PhD thesis, University of Virginia, Charlottesville, Virginia, 2009.

[19] D. L. McDowell, K. Gall, M. F. Horstemeyer, and J. Fan. Microstructure-based fatigue modeling of cast A356-T6 alloy. *Engineering Fracture Mechanics*, 70:49–80, January 2003.

[20] K. Gall, M. F. Horstemeyer, B. W. Degner, D. L. Mcdowell, and J. Fan. On the driving force for fatigue crack formation from inclusions and voids in a cast A356 aluminum alloy. *International Journal of Fracture (Netherlands)*, 108(3):207–233, Apr. 2001.

[21] Y. Xue, D. L. McDowell, M. F. Horstemeyer, M. H. Dale, and J. B. Jordon. Microstructure-based multistage fatigue modeling of aluminum alloy 7075-T651. *Engineering Fracture Mechanics*, 74(17):2810–2823, Nov. 2007.

[22] Jixi Zhang, Rajesh Prasannavenkatesan, Mahesh M. Shenoy, and David L. McDowell. Modeling fatigue crack nucleation at primary inclusions in carburized and shot-peened martensitic steel. *Engineering Fracture Mechanics*, 76(3):315 – 334, 2009.

[23] V. P. Bennett and D. L. McDowell. Polycrystal orientation distribution effects on microslip in high cycle fatigue. *International Journal of Fracture*, 25:27–39, 2003.

[24] S. Kalnaus and Y. Jiang. Fatigue life prediction of copper single crystals using a critical plane approach. *Engineering Fracture Mechanics*, 73:684–696, 2006.

[25] A. M. Korunsky, D. Dini, F. P. E. Dunne, and M. J. Walsh. Comparative asssessment of dissipated energy and other fatigue criteria. *International Journal of Fracture*, 29:1990–1995, 2007.

[26] S. Groh, S. Olarnrithinum, W.A. Curtin, A. Needleman, V.S. Deshpande, and E. Van der Giessen. Fatigue crack growth from a cracked elastic particle into a ductile matrix. *Philosophical Magazine*, 88(30-32):3565–3583, 2008.

[27] H.H.M. Cleveringa, E. Van der Giessen, and A. Needleman. A discrete dislocation analysis of mode i crack growth. *Journal of the Mechanics and Physics of Solids*, 48(6-7):1133–1157, 2000.

[28] J. Lankford, D. L. Davidson, and K. S. Chan. The influence of crack tip plasticity in the growth of small fatigue cracks. *Metallurgical Transactions*, 15A:1579–1588, 1984.

[29] P. J. Laz and B. M. Hillberry. Fatigue life prediction from inclusion initiated cracks. *International Journal of Fatigue*, 20(4):263 – 270, 1998.

[30] K. Tanaka and T. Mura. A theory of fatigue crack initiation at inclusions. *Metall. Trans A*, 13A(1):117–123, Jan. 1982.

[31] G. P. Potirniche and S. R. Daniewicz. Finite element modeling of microstructurally small cracks using single crystal plasticity. *International Journal of Fatigue*, 25(9):877–884, 2003.

[32] K. Tanaka and T. Mura. Fatigue crack growth along planar slip bands. *Acta Metall*, 32(10):1731–1740, Oct. 1984.

[33] K. Tanaka and T. Mura. A dislocation model for fatigue crack initiation. *Journal of Applied Mechanics (Transactions of the ASME)*, 48(1):97–103, Mar. 1981.

[34] K. Matouš and A.M. Maniatty. Finite element formulation for modeling large deformations in elasto-viscoplastic polycrystals. *International Journal for Numerical Methods in Engineering*, 60:2313–2333, 08/01 2004.

[35] R. P. Skelton. Energy criterion for high temperature low cycle fatigue failure. *Materials Science and Technology*, 7(5):427–439, 1991.

[36] A. Fatemi and D. F. Socie. A critical plane approach to multiaxial fatigue damage including out-of-phase loading. *Fat. Fract. Eng. Mater. Struct*, 11(3):149–165, 1988.

[37] M. W. Brown and K. J. Miller. A theory for fatigue failure under multiaxial stress-strain conditions. *Proceedings Institution of Mechanical Engineers*, 187:745–755, 1973.

[38] M. A. Tschopp and D. L. McDowell. Influence of single crystal orientation on homogeneous dislocation nucleation under uniaxial loading. *Journal of the Mechanics and Physics of Solids*, 56(5):1806–1830, May 2008.

[39] D. Fridline. Bethpage, NY: Northrop Grumman Corp. personal communication, 2007.

[40] J. R. Rice, D. E. Hawk, and R. J. Asaro. Crack tip fields in ductile crystals. *International Journal of Fracture*, 42(4):301–321, 04/01 1990.

[41] M. Janssen, J. Zuidem, and R. Wanhill. *Fracture Mechanics*, chapter 12. Spon Press, 2nd edition, 2002.